OBSERVATIONS OF THE
SOLAR WIND-MAGNETOSPHERE-IONOSPHERE COUPLING

Liisa Juusola

Department of Physics
Faculty of Science
University of Helsinki
Helsinki, Finland

Title

Observations of the solar wind-magnetosphere-ionosphere coupling

Abstract

In this thesis, the solar wind-magnetosphere-ionosphere coupling is studied observationally, with the main focus on the ionospheric currents in the auroral region. The thesis consists of five research articles and an introductory part that summarises the most important results reached in the articles and places them in a wider context within the field of space physics.

Ionospheric measurements are provided by the International Monitor for Auroral Geomagnetic Effects (IMAGE) magnetometer network, by the low-orbit CHAllenging Minisatellite Payload (CHAMP) satellite, by the European Incoherent SCATter (EISCAT) radar, and by the Imager for Magnetopause-to-Aurora Global Exploration (IMAGE) satellite. Magnetospheric observations, on the other hand, are acquired from the four spacecraft of the Cluster mission, and solar wind observations from the Advanced Composition Explorer (ACE) and Wind spacecraft.

Within the framework of this study, a new method for determining the ionospheric currents from low-orbit satellite-based magnetic field data is developed. In contrast to previous techniques, all three current density components can be determined on a matching spatial scale, and the validity of the necessary one-dimensionality approximation, and thus, the quality of the results, can be estimated directly from the data. The new method is applied to derive an empirical model for estimating the Hall-to-Pedersen conductance ratio from ground-based magnetic field data, and to investigate the statistical dependence of the large-scale ionospheric currents on solar wind and geomagnetic parameters. Equations describing the amount of field-aligned current in the auroral region, as well as the location of the auroral electrojets, as a function of these parameters are derived. Moreover, the mesoscale (10-1000 km) ionospheric equivalent currents related to two magnetotail plasma sheet phenomena, bursty bulk flows and flux ropes, are studied. Based on the analysis of 22 events, the typical equivalent current pattern related to bursty bulk flows is established. For the flux ropes, on the other hand, only two conjugate events are found. As the equivalent current patterns during these two events are not similar, it is suggested that the ionospheric signatures of a flux rope depend on the orientation and the length of the structure, but analysis of additional events is required to determine the possible ionospheric connection of flux ropes.

ILMATIETEEN LAITOS

Nimeke

Havaintoja aurinkotuulen, magnetosfäärin ja ionosfäärin kytkennästä

Tiivistelmä

Tässä väitöskirjassa tarkastellaan aurinkotuulen, magnetosfäärin ja ionosfäärin kytkentää mittaushavaintojen pohjalta keskittyen ionosfäärivirtoihin revontulialueella. Väitöskirja koostuu viidestä tutkimusartikkelista ja johdanto-osasta, jossa kootaan yhteen artikkelien tärkeimmät tulokset ja asetetaan ne laajempaan asiayhteyteen avaruusfysiikan piirissä.

Ionosfäärimittaukset ovat peräisin International Monitor for Auroral Geomagnetic Effects (IMAGE) -magnetometriverkosta, matalalla kiertävästä CHAllenging Minisatellite Payload (CHAMP) -satelliitista, European Incoherent SCATter (EISCAT) -tutkasta ja Imager for Magnetopause-to-Aurora Global Exploration (IMAGE) -satelliitista. Magnetosfäärimittaukset taas saadaan neljästä Cluster-satelliitista ja aurinkotuulihavainnot Advanced Composition Explorer (ACE) ja Wind -satelliiteista.

Tutkielman puitteissa kehitetään uusi menetelmä ionosfäärivirtojen määrittämiseksi matalalla kiertävän satelliitin mittaamasta magneettikentästä. Toisin kuin aiemmissa tekniikoissa, kaikki kolme virrantiheyden komponenttia voidaan määrittää samalla tarkkuudella, ja vaadittavan yksiulotteisuusoletuksen paikkansapitävyyttä, ja siten tulosten laatua, voidaan arvioida suoraan mittausdatasta. Uutta menetelmää soveltaen kehitetään kokeellinen malli Hallin ja Pedersenin johtavuuksien suhteen arvioimiseksi maanpinnalta mitatusta magneettikentästä, ja tutkitaan tilastollisesti suurikokoisten ionosfäärivirtojen riippuvuutta aurinkotuulen ja geomagneettisista parametreista. Yhtälöt johdetaan kuvaamaan kentänsuuntaisen virran määrää revontulialueella sekä elektrojettien sijainteja näiden parametrien funktiona. Lisäksi tutkitaan keskikokoisia (10-1000 km) ionosfäärin ekvivalenttivirtoja, jotka liittyvät magnetosfäärin pyrstön plasmalevyssä esiintyviin nopeisiin virtauksiin ja vuoköysiin. 22 tapahtuman analyysin perusteella määritetään tyypillinen nopeisiin virtauksiin liittyvä ionosfäärin ekvivalenttivirtakuvio. Vastaavan kuvion löytäminen vuoköysille osoittautuu haasteelliseksi, sillä sopivia tapahtumia löytyy ainoastaan kaksi kappaletta. Koska ekvivalenttivirtakuviot näiden tapahtumien aikana eivät vastaa toisiaan, ehdotetaan, että vuoköysiin liittyvät ionosfääri-ilmiöt riippuvat vuoköysirakenteen pituudesta ja suuntautumisesta, mutta vuoköysien ionosfäärikytkennän lopullinen määrittäminen edellyttää vielä useampien tapahtumien analyysiä.

Contents

Preface

Helsinki, March 2009
Liisa Juusola

Acronyms

AACGM	Altitude Adjusted Corrected GeoMagnetic coordinate system
ACE	Advanced Composition Explorer
AE	Auroral Electrojet index
BBF	Bursty Bulk Flow
CD	Current Disruption
CF	Curl-Free
CGM	Corrected GeoMagnetic coordinate system
CHAMP	CHAllenging Minisatellite Payload
CIS	Cluster Ion Spectrometry experiment
CME	Coronal Mass Ejection
DF	Divergence-Free
DNL	Distant Neutral Line
EISCAT	European Incoherent SCATter
ESA	European Space Agency
ESR	EISCAT Svalbard Radar
FAC	Field-Aligned Current
FGM	FluxGate Magnetometer
FR	Flux Rope
FUV	Far UltraViolet
GEO	GEOgraphic coordinate system
GSE	Geocentric Solar Ecliptic coordinate system
GSM	Geocentric Solar Magnetospheric coordinate system
HIA	Hot Ion Analyser
IGRF	International Geomagnetic Reference Field
IMAGE	Imager for Magnetopause-to-Aurora Global Exploration
IMAGE	International Monitor for Auroral Geomagnetic Effects
IMF	Interplanetary Magnetic Field
LT	Local Time

MAG	GeoMAgnetic coordinate system
MHD	MagnetoHydroDynamics
MIRACLE	Magnetometers - Ionospheric Radars - Allsky Cameras Large Experiment
MLT	Magnetic Local Time
NASA	National Aeronautics and Space Administration
NENL	Near-Earth Neutral Line
PS	Plasma Sheet
PSBL	Plasma Sheet Boundary Layer
SMC	Steady Magnetospheric Convection
SSC	Storm Sudden Commencement
T89	Tsyganenko (1989) magnetic field model
R1	Region 1
R2	Region 2
SCW	Substorm Current Wedge
SECS	Spherical Elementary Current System
SW	Solar Wind
TCR	Travelling Compression Region
UHF	Ultra High Frequency
UT	Universal Time
VHF	Very High Frequency
WIC	Wideband Imaging Camera
WTS	Westward Travelling Surge
1-D	1-Dimensional
2-D	2-Dimensional
3-D	3-Dimensional

Symbols

α	Hall-to-Pedersen conductance ratio
$\mathbf{B}$	Magnetic field
$\mathbf{E}$	Electric field
c	Speed of light
e	Unit charge
ϵ_0	Electric permittivity of free space
I	Electric current
$\mathbf{j}$	Current density
$j_{\parallel}$	Current density parallel to $\mathbf{B}$
$j_{df,r}$	Curl of equivalent current density
$\mathbf{J}$	Surface current density
$\mathbf{J}_{cf}, \mathbf{J}_{df}$	Curl-free and divergence-free part of current density
k_B	Boltzmann constant
μ_0	Magnetic permeability of free space
m_e, m_i	Elecron and ion mass
N	Number density
ν_{en}, ν_{in}	Electron-neutral and ion-neutral collision frequency
ω_{ce}, ω_{ci}	Cyclotron frequency for electrons and for ions
P	Pressure
R_E	Earth radius
R_m	Magnetic Reynolds number
ρ	Mass density
σ	Electric conductivity
σ_H, σ_P	Hall and Pedersen conductivity
$\sigma_{\parallel}$	Conductivity parallel to $\mathbf{B}$
Σ_H, Σ_P	Hall and Pedersen conductance
$\mathbf{V}$	Velocity
t	Time
$\hat{\mathbf{e}}_{\parallel}, \hat{\mathbf{e}}_{\perp}$	Unit vectors parallel and perpendicular to $\mathbf{B}$
$x, y, z, \hat{\mathbf{e}}_x, \hat{\mathbf{e}}_y, \hat{\mathbf{e}}_z$	Cartesian coordinates and unit vectors
$r, \theta, \phi, \hat{\mathbf{e}}_r, \hat{\mathbf{e}}_\theta, \hat{\mathbf{e}}_\phi$	Spherical coordinates and unit vectors

Coordinate systems

The coordinate systems described here are all geocentric, which means that the origin is at the centre of the Earth.

GEO   The z-axis of the geographic coordinate system is parallel to the Earth's rotation axis. The x-axis passes through the Greenwich meridian (0° longitude), and the y-axis completes the right-handed orthogonal set [13].

MAG   The z-axis of the geomagnetic coordinate system is antiparallel to the Earth's magnetic dipole axis (the south pole of the dipole is in the northern hemisphere and the north pole in the southern hemisphere). The x-axis passes through the meridian containing the south pole of the dipole, and the y-axis completes the right-handed orthogonal set [13].

GSE   The z-axis of the the geocentric solar ecliptic coordinate system is parallel to the ecliptic pole. The x-axis points from the Earth towards the Sun, and the y-axis completes the right-handed orthogonal set [13].

GSM   The x-axis of the geocentric solar magnetospheric coordinate system points from the Earth towards the Sun. The y-axis is perpendicular to the Earth's magnetic dipole so that the x-z plane contains the dipole axis. The z-axis is positive towards the hemisphere containing the south pole of the magnetic dipole [13].

CGM   The corrected geomagnetic coordinates (latitude, longitude) of a point in space are computed by tracing the IGRF magnetic field line through the specified point to the dipole geomagnetic equator, then returning to the same altitude along the dipole field line and assigning the obtained dipole latitude and longitude as the CGM coordinates to the starting point (Gustafsson et al., 1992).

AACGM   The altitude adjusted corrected geomagnetic coordinates of a point in space are obtained similar to CGM coordinates, except that the dipole field line is traced to zero altitude instead of the altitude of the starting point.

Publications

This thesis consists of an introductory part and five research articles. The introduction contains a brief background for the research and the most important results reached in the articles. Original abstracts of the publications are listed below.

PUBL. I

Juusola, L., Amm, O., and Viljanen, A., "1D spherical elementary current systems and their use for determining ionospheric currents from satellite measurements," *Earth Planets Space,* **58,** 667–678, 2006.

Abstract. The method of 1D spherical elementary current systems (SECS) is a new way for determining ionospheric and field-aligned currents in spherical geometry from magnetic field measurements made by a low-orbit satellite. In contrast to earlier methods, the full ionospheric current distribution, including both divergence-free and curl-free horizontal currents, as well as field-aligned currents, can be determined. Placing infinitely many 2D SECSs of identical amplitudes at a constant latitude results in two types of 1D SECSs, which are independent of longitude, and by superposition can reproduce any ionospheric and field-aligned current system with the same property. One type of the 1D SECSs is divergence-free and toroidal with a poloidal magnetic field, and the other type is curl-free and poloidal. Associated with the divergence of the curl-free type are radial currents. The magnetic field of the combined curl-free 1D SECS and field-aligned currents is toroidal and restricted to the region above the ionosphere. Ionospheric currents are determined by placing several 1D SECSs at different latitudes and choosing their amplitudes in such a way that their combined magnetic field as closely as possible fits the one measured by the satellite. The 1D SECS method has been tested using both modeled and real data from the CHAMP satellite, and found to work excellently in 1D cases.

PUBL. II

Juusola, L., Amm, O., Kauristie, K., and Viljanen, A., "A model for estimating the relation between the Hall to Pedersen conductance ratio and ground magnetic data derived from CHAMP satellite statistics," *Ann. Geophys.,* **25,** 721–736, 2007.

Abstract: The goal of this study is to find a way to statistically estimate the Hall to Pedersen conductance ratio α from ground magnetic data. We use vector magnetic data from the CHAMP satellite to derive this relation. α is attained from magnetic satellite data using the 1-D Spherical Elementary Current Systems (SECS). The ionospheric equivalent current density can either be computed from ground or satellite magnetic data. Under the required 1-D assumption, these two approaches are shown to be equal, which leads to the advantage that the statistics are not restricted to areas covered by ground data. Unlike other methods, using magnetic satellite measurements to determine α ensures reliable data over long time sequences. The statistical study, comprising over 6000 passes between 55° and 76.5° northern geomagnetic latitude during 2001 and 2002, is carried out employing data from the CHAMP satellite. The data are binned according to activity and season. In agreement with earlier studies, values between 1 and 3 are typically found for α. Good compatibility is found, when α attained from CHAMP data is compared with EISCAT radar measurements. The results make it possible to estimate α from the east-west equivalent current density J_ϕ [A/km]: $\alpha = 2.07/(36.54/|J_\phi| + 1)$ for $J_\phi < 0$ (westward) and $\alpha = 1.73/(14.79/|J_\phi| + 1)$ for $J_\phi > 0$ (eastward). Using the same data, statistics of ionospheric and field-aligned current densities as a function of geomagnetic latitude and MLT are included. These are binned with respect to activity, season and IMF B_z and B_y. For the first time, all three current density components are simultaneously studied this way on a comparable spatial scale. With increasing activity, the enhancement and the equatorward expansion of the electrojets and the R1 and R2 currents is observed, and in the nightside, possible indications of a Cowling channel appear. During southward IMF B_z, the electrojets and the R1 and R2 currents are stronger and clearer than during northward B_z. IMF B_y affects the orientation of the pattern.

PUBL. III

Juusola, L., Amm, O., Frey, H. U., Kauristie, K., Nakamura, R., Owen, C. J., Sergeev, V., Slavin, J. A., and Walsh, A., "Ionospheric signatures during a magnetospheric flux rope event," *Ann. Geophys.,* **26,** 3967–3977, 2008.

Abstract: On 13 August 2002, during a substorm, Cluster encountered two earthward moving flux ropes (FR) in the central magnetotail. The first FR was observed during the expansion phase of the substorm, and the second FR during the recovery phase. In the conjugate ionospheric region in Northern Fennoscandia, the ionospheric equivalent currents were observed by the MIRACLE network and the auroral evolution was monitored by the Wideband Imaging Camera (WIC) on-board the IMAGE satellite. Extending the study of Amm et al. (2006), we examine and compare the possible ionospheric signatures associated with the two FRs. Amm et al. studied the first event in detail and found that the ionospheric footprint of Cluster coincided with a region of downward field-aligned current. They suggested that this region of downward current, together with a trailing region of upward current further southwestward, might correspond to the ends of the FR. Unlike during the first FR, however, we do not see any clear ionospheric features associated with the second one. In the GSM xy-plane, the first flux rope axis was tilted with respect to the y-direction by 29°, while the second flux rope axis was almost aligned in the y-direction, with an angle of 4° only. It is possible that due to the length and orientation of the second FR, any ionospheric signatures were simply mapped outside the region covered by the ground-based instruments. We suggest that the ground signatures of a FR depend on the orientation and the length of the structure.

PUBL. IV

Abstract: The effects of the solar wind dynamic pressure (P), the z component of the solar wind magnetic field (B_z), the merging electric field (E_m), season and the K_p index on R1 and R2 field-aligned currents are studied statistically using magnetic field data from the CHAMP satellite during 2001–2005. The ionospheric and field-aligned currents are determined from the magnetic field data by the recently developed 1-D Spherical Elementary Current System (SECS) method. During southward IMF, increasing $|B_z|$ is observed to clearly increase the total field-aligned current, while during northward IMF, the amount of field-aligned current remains fairly constant regardless of $|B_z|$. The dependence of the field-aligned current on B_z is given by $|I_r[\text{MA}]| = 0.054 \cdot B_z[\text{nT}]^2 - 0.34 \cdot B_z[\text{nT}] + 2.4$. With increasing P, the intensity of the field-aligned current is also found to increase accord-

ing to $|I_r[\text{MA}]| = 0.62 \cdot P[\text{nPa}] + 1.6$, and the auroral oval is observed to move equatorward. Increasing E_m produces similar behaviour, described by $|I_r[\text{MA}]| = 1.41 \cdot E_m[\text{mV/m}] + 1.4$. While the absolute intensity of the ionospheric current is stronger during negative than during positive B_z, the relative change in the intensity of the currents produced by a more intense solar wind dynamic pressure is observed to be approximately the same regardless of the B_z direction. Increasing K_p from 0 to $\geq$5 widens the auroral oval and moves it equatorward from between 66°–74° AACGM latitude to 59°–71° latitude. The total field aligned current as a function of K_p is given by $|I_r[\text{MA}]| = 1.1 \cdot K_p + 0.6$. In agreement with previous studies, total field-aligned current in the summer is found to be 1.4 times stronger than in the winter.

PUBL. V

Juusola, L., Nakamura, R., Amm, O., Kauristie, K., "Conjugate ionospheric equivalent currents during bursty bulk flows," *J. Geophys. Res.,* **114,** A04313, doi:10.1029/2008JA013908, 2009.

Abstract: Ionospheric equivalent currents related to bursty bulk flows (BBF) during Cluster and the International Monitor for Auroral Geomagnetic Effects (IMAGE) magnetometer network conjunctions between 2001 and 2006 are studied. A geomagnetically southeast-northwest aligned, relatively narrow channel of northwestward equivalent current density with downward field-aligned current at its northeastward flank and upward field-aligned current at its southwestward flank is confirmed as the ionospheric signature of BBFs in the majority of cases, i.e., whenever an ionospheric signature is present. Unlike in previous event studies, all conjugate BBFs between 2001 and 2006 are analyzed and during 19 out of 22 BBFs, the channel is observed in the ionosphere. The mean duration of the BBFs observed when the footprint of Cluster is located close to the poleward boundary of the auroral oval is clearly longer (17 min) than the that of the BBFs observed close to the equatorward boundary of the oval (3 min). A superposed epoch analysis of the local IMAGE AE (IE) index reveals a stronger activity level preceding a substorm-related than a nonsubstorm BBF. After the BBF observation, however, the activity in both cases is on the same level as that preceding the substorm BBF observation. The observation of the substorm BBF coincides with a substorm-like disturbance of the IE, while the observation of the nonsubstorm BBF coincides with a step-like increase of the IE.

In PUBL. I–V, the author performed the data analysis and wrote the manuscripts with the assistance of the co-authors. PUBL. I was carried out according to guidelines given by the co-authors. The topics of PUBL. II, III and IV came from the co-authors, as well as help with the interpretation of the results, but the analysis and writing were mainly carried out according to the views of the author. The topic for PUBL. V was suggested by the author.

Chapter 1

Introduction

Space physics is the study of natural plasma environments located close enough to the Earth that they can be probed by in-situ measurements. Such environments encompass the Sun, solar wind and planetary magnetospheres and ionospheres. A magnetosphere is a cavity in the solar wind formed by the interaction of the solar wind with the intrinsic magnetic field or the ionised upper atmosphere of a planet. For the Earth, Jupiter, Saturn, Uranus, and Neptune, the interaction is dominated by a strong intrinsic quasidipolar magnetic field. Venus, on the other hand, has no instrinsic magnetic field, and Mars only has a small remanent field, and therefore their magnetospheres are formed by the interaction of the atmosphere and ionosphere with the solar wind flow. Mercury has a small intrinsic field but no atmosphere; there the solar wind interacts directly with the surface (e.g., Pulkkinen, 2007). The manifestations of space physics phenomena occuring at different planets depend on the magnitude of the instrinsic magnetic field, the existence and characteristics of the planetary atmosphere and ionosphere and the properties of the solar wind, determined by the distance from the Sun. The most abundant observations are naturally available of the terrestrial plasma environment, which can thus be regarded as a "laboratory" for the study the properties of space plasmas. For instance, several impulsive energy release events, such as solar flares and coronal mass ejections, share similar features with magnetospheric substorms. Of all these, the only one that can be investigated in detail with in-situ measurements is the substorm. As mankind has become increasingly dependent on technology, also understanding of the effects of the space physics phenomena on human technology, termed space weather, has become increasingly necessary. A beautiful manifestation of the space physics processes are the auroras occuring in the high latitude ionosphere.

In this thesis, we have treated the terrestrial plasma environment, which is characterized by a strong intrinsic magnetic field and a dense atmosphere and ionosphere. Moreover, we have concentrated on the ionospheric currents in the

auroral region. The main scientific objectives to be reached within the framework of this thesis were:

1. To develop a new Spherical Elementary Current System -based method for determining ionospheric currents from low-orbit satellite-based magnetic field measurements. Unlike previous techniques, the method would allow for the determination of all three components of the ionospheric current density (PUBL. I and II).

2. To apply the new method to develop a way to statistically estimate the Hall-to-Pedersen conductance ratio from ground-based magnetic data (PUBL. II).

3. To apply the new method to study statistically the dependence of the large-scale ionospheric currents on solar wind and geomagnetic parameters (PUBL. II and IV).

4. To study the meso-scale (100–1000 km) ionospheric currents, determined from ground-based magnetic measurements using the Spherical Elementary Current Systems, and their connection to magnetospheric plasma sheet structures. In particular, the typical ionospheric equivalent current patterns related to bursty bulk flows (PUBL. V) and flux ropes (PUBL. III) were to be determined.

This Chapter contains an introduction to solar wind-magnetosphere-ionosphere coupling. We begin with a brief review of the basic plasma physics concepts relevant to the topic, then move on to the properties of the solar wind, the magnetosphere, the ionosphere, and their mutual interactions. In Chapter 2, dynamical processes, such as geomagnetic storms and substorms, are reviewed, and Chapter 3 contains a brief description of the instruments whose data have been utilised in PUBL. I–V. In Chapter 4, the use of Spherical Elementary Current Systems for determining ionospheric currents from magnetic measurements is discussed, and Chapter 5 presents features of the ionospheric currents at different spatial and temporal scales. The final Chapter 6 contains conclusions and an outlook.

1.1   Basic plasma physics

Plasma is quasineutral gas containing enough free charges so that collective phenomena, controlled by electric and magnetic fields, become important to its physical behaviour. Quasineutrality means that a macroscopic plasma element contains, on average, equal numbers of positive and negative charges.

Macroscopic plasma physics is often described in terms of magnetohydrodynamics (MHD). In MHD, magnetized plasma is treated as a continuous medium described by a single temperature, number density and bulk velocity. Ohm's law in MHD

$$\mathbf{E} + \mathbf{V} \times \mathbf{B} = \mathbf{j}/\sigma, \tag{1.1}$$

where $\mathbf{E}$ is the electric field, $\mathbf{B}$ the magnetic field, $\mathbf{V}$ the bulk velocity of the plasma, $\mathbf{j}$ the current density, and σ the conductivity, can be combined with the Maxwell equations

$$\nabla \cdot \mathbf{B} = 0 \tag{1.2}$$

$$\nabla \times \mathbf{E} = -\frac{\partial \mathbf{B}}{\partial t} \tag{1.3}$$

$$\nabla \times \mathbf{B} = \mu_0 \mathbf{j} + \frac{1}{c^2}\frac{\partial \mathbf{E}}{\partial t} \approx \mu_0 \mathbf{j} \tag{1.4}$$

as the induction equation

$$\frac{\partial \mathbf{B}}{\partial t} = \nabla \times (\mathbf{V} \times \mathbf{B}) + \frac{1}{\mu_0 \sigma}\nabla^2 \mathbf{B}, \tag{1.5}$$

which describes the temporal changes of the magnetic field due to convection and diffusion. The relative strengths of convection and diffusion are described by the magnetic Reynolds number $R_m = \mu_0 \sigma L_B V$, where L_B is the local magnetic field gradient length scale.

In a collisionless plasma, $\sigma \to \infty$ and $R_m \gg 1$. Convection then dominates over diffusion, and the magnetic field moves together with the plasma, such that two plasma elements initially occupying a common field line will remain on a common field line. The magnetic field is said to be frozen-in to the motion of the plasma. The identity of a field line is then determined by the chain of plasma elements occupying it, and the motion of the plasma elements perpendicular to the magnetic field can also be thought of as the motion of the field line. In such plasmas, the electric field is given by the ideal MHD Ohm's law

$$\mathbf{E} = -\mathbf{V} \times \mathbf{B}, \tag{1.6}$$

and the plasma velocity by

$$\mathbf{V} = \frac{\mathbf{E} \times \mathbf{B}}{B^2}. \tag{1.7}$$

This $\mathbf{E} \times \mathbf{B}$-drift is independent of the mass and the charge of the particles and, thus, does not create electric current.

Although the ideal MHD generally describes well the behavior of the plasma in the solar wind, magnetosheath and outer magnetosphere, there are regions

where the frozen-in condition breaks down. If the velocity of the plasma slows down, or the local magnetic field gradient length scale becomes small, or some process, such as collisions, wave-particle interactions or plasma turbulence, causes resistivity, diffusion of the magnetic field becomes relevant.

Reconnection is a local breaking of the frozen-in condition and, thus, requires both convection and diffusion. Reconnection refers to a process during which two plasma elements that initially occupied a common field line end up on separate field lines, that is, their magnetic connection is broken. When two initially separate plasma populations frozen-in to oppositely oriented magnetic fields come into contact with each other, a thin current sheet is formed between them according to Ampère's law. In this limited diffusion region, the frozen-in condition breaks down. An X-line is formed in the middle of the region, where the magnetic field vanishes. In the reconnection process, magnetic energy is converted to the kinetic energy of the plasma so that reconnected plasma is expelled from the diffusion region as two oppositely directed plasma jets. A reverse process that generates electromagnetic energy from plasma motion, on the other hand, is called a dynamo.

1.2 Solar wind

The Sun controls the plasma physics of the entire solar system. In addition to emitting electromagnetic radiation that ionises the neutral atoms and molecules in the atmospheres of the planets and the interstellar gas, fully ionised, magnetised plasma flows away from it in all directions. This flow is known as the solar wind.

The gravity of the Sun is not strong enough to maintain static equilibrium in the solar corona, which continuously expands outwards into the interplanetary space as the solar wind. The temperature of millions of kelvins in the corona is high enough to strip hydrogen and helium completely of their electrons, and also heavier elements to a large degree. Solar wind is therefore almost fully ionised plasma, consisting mostly of protons and electrons, with about three percent of α-particles and smaller amounts of multiply ionised heavier elements.

Due to the high conductivity of the coronal plasma, the magnetic field freezes-in to it and is carried all the way to the outer reaches of the heliosphere. The solar magnetic field carried by the solar wind is called the interplanetary magnetic field (IMF). While the solar wind streams radially away from the Sun, the footprints of the field lines are attached to the Sun and follow the 27 day rotation. As a consequence, the interplanetary magnetic field is twisted into the so-called Parker spiral.

At the Earth's orbit, the observed average speed of solar wind is about 450 km/s, the proton number density 6.6 cm^{-3}, the electron number density 7.1 cm^{-3},

and the magnitude of the interplanetary magnetic field 7 nT (e.g., Kivelson and Russell, 1995). On average, the Parker spiral forms an angle of 45° with the Sun-Earth-line. However, while the solar wind is flowing continuously, the actual IMF direction, as well as other solar wind properties, fluctuate considerably depending on the solar activity level and coronal structure.

1.3 Magnetosphere

The Earth's magnetic field or geomagnetic field is produced by a dynamo process in the Earth's liquid outer core at a depth of 3000–5000 km. The magnetic field can roughly be approximated as a dipole, with its magnetic north pole located close to the geographic south pole and the magnetic south pole close to the geographic north pole. The angle between the Earth's rotation axis and the dipole axis is about 11° and the magnitude of the field ranges from about 30 μT at the equator to 60 μT at the poles. The offset between the actual observed magnetic pole and the geographic pole is 11.5° in the northern and 14.5° in the southern hemisphere

The interaction of the solar wind with the Earth's magnetic field creates the magnetosphere. It is a cavity in the solar wind surrounding the Earth, where the geomagnetic field dominates the motion of charged particles instead of the interplanetary magnetic field, and around which the solar wind flow is deflected. The boundary separating the magnetosphere from the solar wind is called the magnetopause.

Moreover, since the solar wind speed exceeds that at which information is transferred in the plasma, a shock front is formed around the magnetopause. This bow shock separates the undisturbed solar wind from the shocked flow. On the Sun-Earth line, the bow shock is located at the distance of about 13 Earth radii ($R_E = 6371.2$ km) from the centre of the Earth. Between the bow shock and the magnetopause, the shocked solar wind flows in a region called the magnetosheath.

Close to the Earth, the geomagnetic field still resembles a dipole, but farther away, the solar wind compresses the dayside magnetosphere in in such a way that the magnetopause forms at a distance where the dynamic pressure of the solar wind balances the mainly magnetic pressure of the geomagnetic field. Typical solar wind conditions give to the sunwardmost point of the magnetopause, called the subsolar point, a distance of 10 R_E upstream of the Earth, but under strong solar wind driving the magnetopause can be pushed well inside the geostationary orbit located at 6.6 R_E. At this distance, a satellite orbiting around the Earth has a 24 hour rotation period, and thus remains at a constant location with respect to the Earth's surface. On the nightside, the geomagnetic field is streched to a tail longer than 100 R_E, where the magnetopause is located on average about 30 R_E
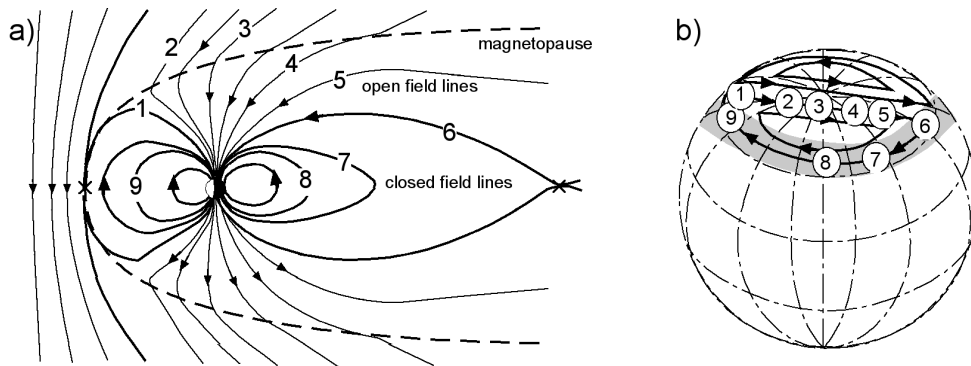
Figure 1.1: Reconnection and field line convection a) in the magnetosphere and b) in the ionosphere. Illustration by Minna Palmroth after Dungey (1961).

from the Sun-Earth line.

1.3.1 Convection

Fig. 1.1a illustrates schematically field line convection in the magnetosphere during southward IMF. The regions where reconnection takes place at the dayside magnetopause and in the distant tail are marked by X. When southward IMF encounters the northward oriented geomagnetic field at the dayside magnetosphere, reconnection occurs (field line 1 in Fig. 1.1a). The newly reconnected, so-called "open" field lines have one end attached to the Earth and one to the solar wind. Both halves of the reconnected dipole field line are dragged tailwards, one across the northern, the other across the southern polar cap with the solar wind flow (2–5 in Fig. 1.1a). According to Eq. (1.6), the solar wind flow imposes a dawn-to-dusk directed electric field across the polar cap. In the distant tail, the additional magnetic flux forces the field lines to move towards the equatorial plane, where the oppositely directed field lines from the northern and southern hemispheres reconnect again at the so-called distant neutral line (DNL) at the distance of about 100–200 R_E from the Earth (6 in Fig. 1.1a). When the two open field lines merge, the resulting closed, but far streched field line convects back toward the dayside magnetopause (7–9 in Fig. 1.1a), while the other convects antisunward to rejoin with the solar wind flow.

The solar wind energy enters the magnetosphere by magnetic reconnection and viscous interaction (Dungey, 1961; Axford and Hines, 1961), but the location where reconnection takes place on the dayside magnetopause still remains unresolved. There are two main hypothesis that predict the effect of the IMF direction on the location: According to the component reconnection hypothesis

Tail lobe

Plasma sheet

Cross-tail
current

Ring current

Magnetopause
current
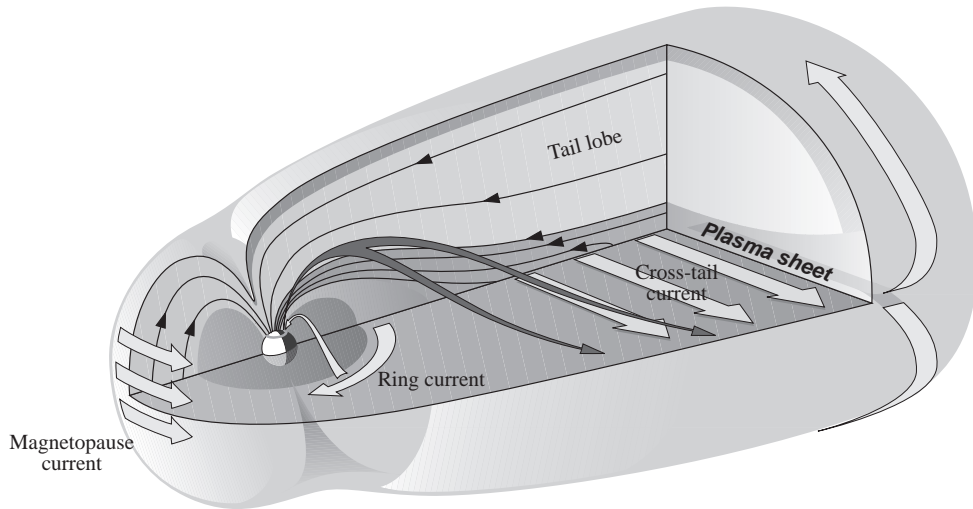
Figure 1.2: Sketch of the Earth's magnetosphere and large scale current systems. Illustration by Teemu Mäkinen.

(Sonnerup, 1974), reconnection is most likely to occur on a line passing through the subsolar point, where the solar wind dynamic pressure is most intense. The angle between the magnetosheath and the geomagnetic field is less relevant: the antiparallel components of the fields are reconnected regardless of the presence of any parallel components. In contrast, the antiparallel reconnection hypothesis (Luhmann et al., 1984) states that the presence of parallel components is enough to prevent reconnection, which implies that reconnection can only take place in those regions on the magnetopause where the magnetosheath and geomagnetic fields are oppositely directed. Therefore, any IMF orientation can produce reconnection, provided that there is a region where the two fields are antiparallel, and that there is sufficient plasma convection towards that region to bring the two field configurations in contact. During negative IMF B_z (in GSM coordinates) and zero B_y, both hypothesis predict a uniform reconnection line at the equatorial plane, but with increasing B_y, the antiparallel reconnection line breaks and the ends move away from equator toward the cusps, while the component reconnection line remains uniform and is merely tilted. During positive B_z, parallel reconnection is predicted to take place tailward of the cusps, while component reconnection occurs mostly due to B_y.

1.3.2 Structure

Fig. 1.2 displays a sketch of the structure of the Earth's magnetosphere and large scale current systems. The magnetopause currents, which on the dayside are also called the Chapman-Ferraro currents, separate the magnetosphere from the solar wind.

For the closed magnetospheric configuration, the funnel-shaped regions between the sunward and tailward directed field lines in both hemispheres are called the polar cusps. The cusps provide the shocked solar wind plasma of the magnetosheath a direct entry to the magnetosphere and to the ionosphere. For the open magnetospheric configuration, the cusps are the narrow regions of recently opened field lines tailward of the last closed field line. The open field lines of the cusps are connected with those of the interplanetary magnetic field, and thus provide the solar wind plasma access to the magnetosphere and to the ionosphere.

Most of the volume of the magnetosphere consists of magnetic flux tubes that are connected to the polar ionospheres at one end and to the interplanetary magnetic field at the other end. These low density regions are called the tail lobes. The magnetic field lines of the northern lobe are connected to the vicinity of the northern magnetic pole, and directed towards the Earth, whereas those of the southern lobe are connected near the southern pole and directed away. A structure like this requires an electric current flowing in the equatorial plane from the dawnside to the duskside. This cross-tail current is closed via magnetopause currents encircling both lobes. Over a large range of distances downstream of about 20 R_E, the fields of the northern and southern tail lobes are nearly antiparallel, and have an almost constant magnetic field intensity of about 20 nT (e.g., Pulkkinen, 2007).

Between the tail lobes lies the plasma sheet (PS), a region of denser plasma, centered at the equator, and typically about 2–6 R_E thick. Plasma densities in the plasma sheet are of the order of 1 cm^{-3} and the magnetic field is weak, only a few nT. Thus, while the ratio of plasma (P) and magnetic pressures $\beta = 2\mu_0 P/B^2$ is very low in the tail lobes, it generally exceeds unity in the central plasma sheet. Field lines of the plasma sheet are closed to the Earth's dipole field at both ends, but streched far into the tail. The region of closed field lines between the tail lobe and the plasma sheet is called the plasma sheet boundary layer (PSBL). The ionospheric regions, where the plasma sheet and the plasma sheet boundary layer are connected are called the auroral ovals.

Inside the geosyncronous orbit at 6.6 R_E from the centre of the Earth, the geomagnetic field is almost dipolar. There are three partly overlapping plasma populations in this region: the plasmasphere, the ring current and the radiation belts. The ring current (e.g., Frank, 1967), located approximately between 2–7 R_E, is created by 10–200 keV ions and electrons trapped on the closed dipolar field lines. Due to curvature and gradient drifts, positive ions of the ring current

drift westward while the negative electrons drift eastward, resulting in a permanent westward electric current. During strong magnetic activity, the ring current is amplified by injection of new particles, while during quiet times the particles slowly dissipate through different processes, and the current weakens.

The trapping regions of high-energy charged particles surrounding the Earth are called the van Allen radiation belts (Allen et al., 1958; Allen and Frank, 1959). The inner belt contains primarily protons with energies exceeding 10 MeV, while the outer belt consists mainly on electrons with energies up to about 10 MeV.

The torus-shaped inmost part of the magnetosphere consists of cold (about 1 eV), dense plasma (10–1000 cm^{-3}) of subauroral ionospheric origin. While the drift of the energetic particles is largely controlled by the magnetic field geometry, the cold plasma particles are guided both by the electric and magnetic fields. The Earth's rotation sets up an electric field, which drags the cold plasma into a corotational motion. The competing effects of this and the solar wind-imposed electric field create a boundary, inside of which particles are trapped on closed orbits around the Earth, while outside, particles follow the magnetospheric convection. In the vicinity of this boundary, located at about 3–5 R_E from the centre of the Earth, plasma density has a sharp gradient. This is known as the plasmapause (e.g., Goldstein et al., 2003), and the region inside it is the plasmasphere.

1.4   Ionosphere

The Earth's ionosphere is the partially ionised upper atmosphere at about 70–1500 km altitude. It is created by solar radiation and particle precipitation that ionise the neutral atmosphere. The ionosphere is located approximately within the same altitude range as the neutral atmospheric layer thermosphere (Fig. 1.3), which thereby provides a background energy and momentum sink for the magnetosphere-ionosphere coupling processes.

The strong geomagnetic field influences charged particles. As a result, the ionospheric plasma is very anisotropic and the ionosphere at low (0–30°), middle (30°–60°) and high latitude (60°–90°) zones exhibits quite different phenomena. At high latitudes, for instance, ionisation by particle impact is important. In this thesis, we have concentrated mainly on the auroral region in the high latitude ionosphere.

1.4.1   Structure

Due to the ambient collisional neutral atmosphere, the ionospheric electron density profile is dependent on the balance between the creation and destruction of
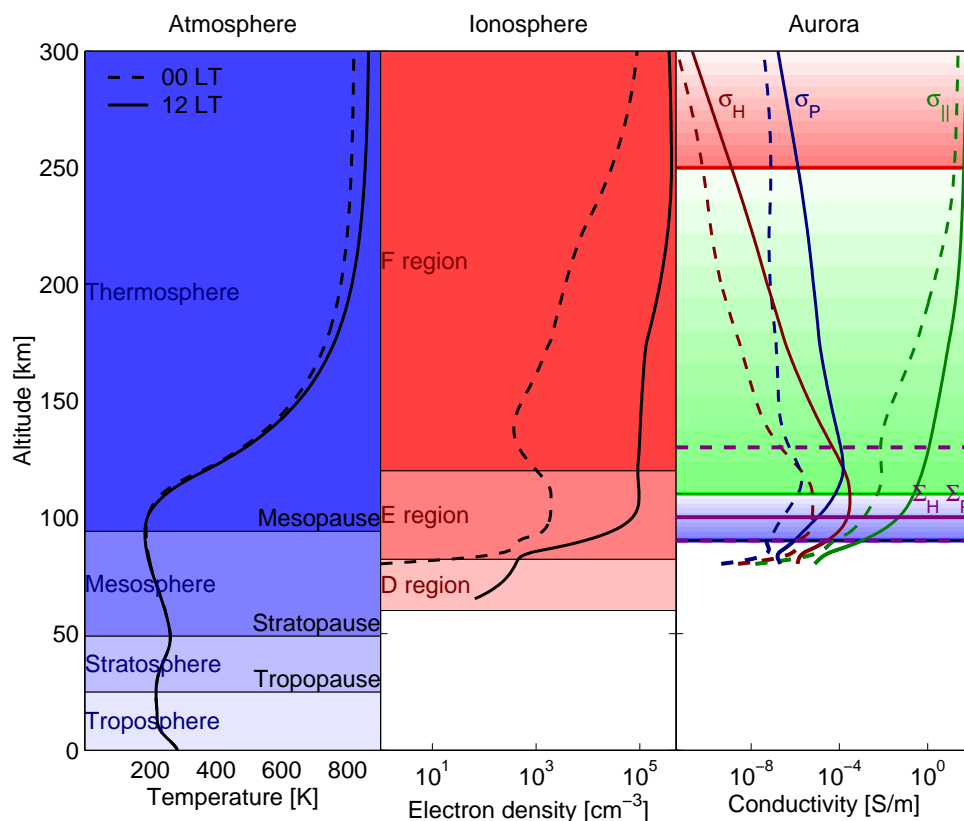
Figure 1.3: *Left:* Modeled neutral temperature as a function of altitude above Helsinki on 22 September 2005 at 00 and 12 local time (from [01]) and the resulting atmospheric layers. *Middle:* Modeled ionospheric electron density (from [02]) and ionospheric layers. *Right:* Modeled ionospheric conductivities (from [03], see Sect. 1.4.2) and the main colors typically observed in auroral light (see Sect. 1.4.1). The dashed purple lines mark the altitude range where the majority of the perpendicular currents are concentrated (Sect. 1.4.2) and the solid purple line the thin sheet (Sect. 1.4.3).

ions and electrons, that is, between ionisation and recombination. Most of the ionisation is caused by the solar EUV radiation at wavelengths 10–100 nm. In the auroral region, another important source of ionisation, particularly during nighttime, is the flux of energetic particles. This particle precipitation is highly irregular, with large spatial and temporal variations.

Charged particles, mostly electrons, precipitating into the Earth's atmosphere are also responsible for producing auroral light. Collisions with precipitating particles excite atmospheric atoms and molecules to higher energy levels, which then relax by emitting auroral light. Most of the visible auroral light is typically produced by particles with energies of 0.5–20 keV, and is emitted between 100–150 km altitude. The main colors observed in auroral light, and their peak altitudes, are red (630.0 nm) at 250 km altitude, green (557.7 nm) at 110 km altitude and blue (427.8 nm) at 90 km altitude (Brekke, 1997). Red are green are the most commonly occurring emissions, but the red emissions are often much weaker than the green ones. Red and green are produced by electron collisions with atomic oxygen, and blue with nitrogen molecules. Green and blue emissions are caused by higher energy particles than red emissions, capable of penetrating deeper into the atmosphere.

The ionospheric electron density changes as a function of altitude. The resulting layers approximately between 60–90 km, 90–150 km and 150–1500 km are called the D, E and F regions (Fig. 1.3). The altitude where the ionosphere is transformed to the magnetosphere is not rigorously defined, but in the magnetosphere the neutral density begins to be of the same order of magnitude as the electron density, which condition is approximately satisfied at 1500 km altitude. The E region is formed by a local electron density maximum that is on the dayside often produced solely by solar irradiation and on the nightside enhanced by electron precipitation. The global maximum of the altitude profile, on the other hand, is generally located at about 250 km altitude in the F region.

The variation of the solar zenith angle causes both diurnal and seasonal variation in the ionospheric electron density profile. For instance, due to the $23°$ tilt of the Earth's rotation axis, during summer solstice the entire auroral oval is sunlit, while during winter solstice it is in the dark. In the absence of solar radiation, the density of free electrons decreases due to recombination. The effect of the diurnal and seasonal cycles and the about 11-year activity cycle of the Sun on the three ionospheric layers varies significantly. While the E region is much weakened at night, and the D region disappears altogether, the F region is less affected. However, in the auroral region when particle precipitation occurs at night, the D region may exist and the E region is drastically increased with an electron density peak occasionally larger than that of the F region.

1.4.2 Convection and currents

The ionospheric electric field can originate from the solar wind-imposed electric field, the corotation electric field and the electric field produced by the neutral wind dynamo. For now, however, further details of the origin of the ionospheric electric field are omitted, and in this section we concentrate on the effects it has on the ionospheric plasma instead. We return to the question of the origin in Sect. 1.5.1.

The effect the ionospheric electric field has on the plasma depends on altitude (e.g., Schunk and Nagy, 2000). In the F region, the cyclotron frequency is greater than the collision frequency with neutrals for both ions and electrons, which thereby mainly follow the $\mathbf{E} \times \mathbf{B}$ drift. As the altitude decreases, the collision frequency increases with increasing neutral density, and thus the drift velocity rotates from the $\mathbf{E} \times \mathbf{B}$ direction towards $\mathbf{E}$. In the E region, collision frequency is still smaller than cyclotron frequency for electrons, which then mainly follow the $\mathbf{E} \times \mathbf{B}$ drift, but ions are collisional and drift dominantly in the direction of the electric field $\mathbf{E}$. In the D region, both electrons and ions are collisional. In addition to turning the drift velocities of ions and electrons parallel and antiparallel to the electric field, the increasing collision frequences also decrease the magnitudes of these velocities.

The density of electrons (N_e) and ions and their cyclotron frequences (ω_{ce}, ω_{ci}) and collision frequences with neutrals (ν_{en}, ν_{in}) determine the ionospheric electric conductivity. Because of the effect of the geomagnetic field, the conductivity is anisotropic, and therefore three conductivities are defined: parallel conductivity ($\sigma_{\parallel}$), Pedersen conductivity (σ_P) and Hall conductivity (σ_H)

$$\sigma_P = \left(\frac{1}{m_e \nu_{en}} \frac{\nu_{en}^2}{\nu_{en}^2 + \omega_{ce}^2} + \frac{1}{m_i \nu_{in}} \frac{\nu_{in}^2}{\nu_{in}^2 + \omega_{ci}^2} \right) N_e e^2 \qquad (1.8)$$

$$\sigma_H = \left(\frac{1}{m_e \nu_{en}} \frac{\omega_{ce} \nu_{en}}{\nu_{en}^2 + \omega_{ce}^2} - \frac{1}{m_i \nu_{in}} \frac{\omega_{ci} \nu_{in}}{\nu_{in}^2 + \omega_{ci}^2} \right) N_e e^2 \qquad (1.9)$$

$$\sigma_{\parallel} = \left(\frac{1}{m_e \nu_{en}} + \frac{1}{m_i \nu in} \right) N_e e^2, \qquad (1.10)$$

where m_e and m_i are the electron and ion masses, respectively, and e is the unit charge. The Hall conductivity is the conductivity in the direction perpendicular to both the magnetic and electric fields, the Pedersen conductivity in the direction of the electric field component perpendicular to the magnetic field ($\mathbf{E}_\perp$) and the field-aligned conductivity in the direction of the magnetic field. The maxima of the Hall and Pedersen conductivity profiles occur in the E region approximately at 110 km and around 120–130 km altitude, respectively (Fig. 1.3).

Although less than 0.1% of the atmospheric molecules are ionised, the ionosphere is a relatively good conductor, and one of the most significant feature of

the ionosphere is its ability to conduct perpendicular electric currents through a medium of finite conductivity. The electric current arises due to the different drift velocities of ions ($\mathbf{V}_i$) and electrons ($\mathbf{V}_e$)

$$\mathbf{j} = eN_e(\mathbf{V}_i - \mathbf{V}_e). \tag{1.11}$$

In the F region, both ions and electrons $\mathbf{E} \times \mathbf{B}$-drift in the same direction, and therefore do not carry electric current. In this region, both the Hall and Pedersen conductivities decrease rapidly with increasing altitude. Since charged particles are free to move along magnetic field lines, but not across them, the field-aligned conductivity is several orders of magnetide higher. Therefore, even a very small field-aligned electric field can result in significant field-aligned current. In the E region, the difference in the drift velocities of the dominantly collisional ions and the collisionless electrons gives rise to an electric current. The $\mathbf{E} \times \mathbf{B}$-drift of the electrons is accompanied by Hall current in the opposite direction, while the ions carry Pedersen current in the direction of the perpendicular electric field. The field-aligned conductivity is still much higher than the prependicular conductivity. In the D region, the ions drift parallel to the electric field and the electrons antiparallel, which should result in Pedersen current, but the electron and ion densities are so low and collision frequencies so high that the Pedersen conductivity is small. Also the field-aligned conductivity is small, because collisions dominate the particle motion even along field lines. Hence, the majority of the perpendicular ionospheric currents flow in the relatively narrow region between 90 and 130 km altitude (e.g., Kamide and Brekke, 1977), which have been marked in Fig. 1.3 by the dashed purple lines. In the polar regions, field-aligned currents from the magnetosphere can be closed at this altitude via the perpendicular currents. The ionospheric current density in terms of conductances and the electric field is described by Ohm's law

$$\mathbf{j} = \sigma_P \mathbf{E}_\perp + \sigma_H \hat{\mathbf{e}}_{||} \times \mathbf{E}_\perp + \sigma_{||} \mathbf{E}_{||}, \tag{1.12}$$

where $\hat{\mathbf{e}}_{||}$ is a unit vector in the direction of the geomagnetic field.

1.4.3 Thin-sheet approximation

Because the perpendicular ionospheric currents are concentrated in a relatively thin layer between about 90–130 km altitude, they are often modeled as a spherical surface current distribution at a constant altitude of about 100 km (marked in Fig. 1.3 by the solid purple line). Assuming that the electric field remains constant as a function of altitude in this region, the perpendicular part of Ohm's law can be written as

$$\mathbf{J}_\perp = \underbrace{\Sigma_P \mathbf{E}_\perp}_{=\mathbf{J}_P} + \underbrace{\Sigma_H \hat{\mathbf{e}}_{||} \times \mathbf{E}_\perp}_{=\mathbf{J}_H}. \tag{1.13}$$

29

Here, $\mathbf{J}_\perp$ is the perpendicular sheet current density, Σ_H and Σ_P are the height-integrated conductivities, called conductances, and $\mathbf{J}_H$ and $\mathbf{J}_P$ are the Hall and Pedersen height-integrated current density components, respectively.

Above 90 km, the field-aligned conductivity is several orders of magnitude larger than the perpendicular conductivities. Consequently, if a parallel electric field is set up, electrons moving along the field lines can swiftly cancel it out. The parallel electric field is therefore often assumed to vanish, and instead of Ohm's law, the ionospheric field-aligned current density is given by current continuity

$$j_{||} = \nabla \cdot \mathbf{J}_\perp. \tag{1.14}$$

Thus, in the thin sheet approximation, there are two kinds of currents in the ionosphere: perpendicular sheet currents at 100 km altitude, described by Ohm's law, and field-aligned currents above 100 km altitude, described by current continuity.

1.5 Magnetosphere-ionosphere coupling

In the previous section, the ionospheric electric field, precipitating particles, and field-aligned currents were discussed regardless of their origin, but the electric fields and the exchange of both charged and neutral particles couple the magnetosphere and the ionosphere. Energy is transferred from the magnetosphere to the ionosphere and atmosphere via particle precipitation and field-aligned currents. The conversion of electromagnetic energy associated with the perpendicular Pedersen currents to heat is called Joule, Ohmic or frictional heating.

1.5.1 Ionospheric convection electric field

As already mentioned briefly in Sect. 1.4.2, the ionospheric electric field can originate from the solar wind-imposed electric field, the corotation electric field and the electric field produced by the neutral wind dynamo. In this section, these sources are discussed in more detail.

In the ionosphere, inductive electric fields, caused by rapid local changes of current systems and their magnetic fields, are generally expected to be unimportant and hence, for the electric field applies

$$\nabla \times \mathbf{E} = -\frac{\partial \mathbf{B}}{\partial t} = 0. \tag{1.15}$$

If it can further be assumed that the field-aligned electric field $E_{||} = 0$, the highly conducting geomagnetic field lines can be considered as equipotentials and the

magnetospheric electric field (Sect. 1.3.1) can be mapped down to the ionosphere along them.

Although these assumptions provide a good starting point for more detailed interpretations, they are rarely exactly valid. Satellite measurements have shown that particularly in regions of upward field-aligned current, a potential difference is formed between the ionosphere and the magnetosphere. The potential difference corresponds to a very finely structured, upward directed electric field. The electric field accelerates electrons towards the ionosphere, which causes narrow, bright auroral arcs. In regions of downward current, on the other hand, a downward directed electric field prevents the precipitating electrons from reaching the ionosphere, which causes dark stripes, "black auroras", in the diffuse background glow. According to the observations, the field-aligned acceleration takes place between 3000–15000 km altitude. Moreover, Eq. (1.15) does not apply in very dynamical situations, when inductive effects become relevant (Vanhamäki et al., 2007).

In addition to the electric field mapped from the magnetosphere to the ionosphere, also other sources contribute to the ionospheric electric field. For instance, the tendency of the ionospheric plasma to corotate with the Earth gives rise to a corotation electric field (e.g., Schunk and Nagy, 2000). The ionospheric plasma also interacts with the neutral atmosphere through particle collisions. Due to the frequent ion-neutral collision, the ionospheric plasma is dragged across magnetic field lines by the neutral gas (Campbell, 1997). This neutral wind dynamo varies with altitude and is often considered insignificant compared to the magnetospheric dynamo in the E region. It drives magnetic variation called S_q or solar quiet (Chapman and Bartels, 1940).

1.5.2   Conjugate magnetospheric and ionospheric regions

Conjugacy between a magnetospheric and an ionospheric region means that they are located on the same magnetic field line, since the electric field and current between the magnetosphere and the ionosphere are mapped along geomagnetic field lines. Besides magnetosphere-ionosphere coupling, the concept of conjugacy can also be useful when comparing ionospheric observations, such as auroras, occuring in both hemispheres simultaneuously. Naturally, such a comparison is only meaningful in the closed field line region, since the open field lines only have one footprint in the ionosphere. Furthermore, two magnetospheric measurements can also be compared, if they take place somewhere along a common field line.

The circular regions surrounding the magnetic poles are called the polar caps. The solar wind sweeping across the open magnetic field lines connected to these regions creates an electric field according to Eq. (1.6). This electric field, directed from dawn to dusk, maps down to the ionosphere, where at about 100 km altitude

it causes electrons to drift from the dayside to the nightside (2–5 in Fig. 1.1b) and ions from dawn to dusk in both hemispheres. The polar cap size is a measure of the magnetic flux within the tail lobes: increasing the amount of open flux increases the size of the polar cap, while decreasing the amount of open flux decreases it.

The field lines equatorward of the polar cap are closed. The intermediate regions between the open field line regions of the polar caps and the low-latitude region containing the dipolar field lines are called the auroral ovals. The auroral ovals encircle the magnetic poles and host continuous diffuse auroral precipitation in addition to the bright auroral displays associated with events of geomagnetic activity. On the nightside, the field lines of the auroral oval are connected to the plasma sheet. The boundary between the open field lines of the lobes and the closed field lines of the plasma sheet, the plasma sheet boundary layer, maps to the poleward edge of the auroral oval. In the plasma sheet, the plasma flow is directed towards the Earth, on average. Closer to the Earth, the flow is deflected around the dipolar field line region of the inner magnetosphere and continues to the dayside in the dawn and dusk sectors. In the ionosphere, the mapped electric field causes the antisunward electron flow of the polar cap to split in two when it reaches the nightside auroral oval, and return to the dayside in the dawn and dusk sector ovals (6–9 in Fig. 1.1b). The ions, on the other hand, drift from the equatorward boundary of the oval towards the poleward boundary on the duskside, and vice versa on the dawnside. On the nightside and on the dayside, the ion drift is from dawn to dusk. The field lines immediately poleward of the auroral oval centered at the local noon are connected to the polar cusps (1 in Fig. 1.1b).

According to the direction of the IMF, reconnection on the dayside magnetopause can result in either symmetric or asymmetric convection patterns in the two hemispheres. When the IMF is southward ($B_z < 0$ in GSM coordinates), plasma flows antisunward across the polar cap and sunward in the auroral oval, forming a two-cell convection pattern. For $B_y \approx 0$, the pattern is symmetric. For $B_y < 0$, the dawn cell becomes rounder and the dusk cell crescent-shaped, whereas for $B_y > 0$, the dusk cell becomes rounder and the dawn cell crescent-shaped in the northern hemisphere. In the southern hemisphere, for a given sign of B_y, the behaviour of the cells is reversed. When IMF is northward ($B_z > 0$), the convection patterns are more complex, for instance forming multiple cells (e.g., Schunk and Nagy, 2000). During strongly positive B_z, the configurations in the two hemispheres may be very different (Lu et al., 1994).

The drifting electrons carry Hall current in the opposite direction. The predominant features of this component are the regions of strong antisunward directed currents in the dawn and dusk sector auroral ovals, called the electrojets, and the region on the nightside where they meet, called the Harang discontinuity (bottom row of Fig. 1.4). The Pedersen current carried by the ions mainly closes the field-aligned currents flowing between the magnetosphere and the ionosphere

(middle row of Fig. 1.4).

Due to their larger mass, the number of precipitating ions is much smaller than that of the quickly moving electrons, typically 1–2 orders of magnitude (e.g., Schunk and Nagy, 2000) and, therefore, upward field-aligned current is carried mainly by the precipitating electrons. In a steady state, quasineutrality is maintained by the positive ion background along the field lines. The downward return current is provided by upward flowing ionospheric electrons. Statistically, the large-scale field-aligned currents in the auroral region consist of a pair of co-centric rings, called the region 1 (R1) and region 2 (R2) systems (top right hand side panel of Fig. 1.4). The poleward R1 currents flow into the ionosphere on the dawnside and out of the ionosphere on the duskside, whereas the equatorward R2 currents have an opposite polarity at a given local time (Iijima and Potemra, 1976). In general, particle precipitation in the auroral zone is highly structured and time dependent.

The exact mapping of the R1 and R2 field-aligned currents to the magnetosphere is still unresolved. Since the R1 currents lie close to the boundary between the open and closed field lines, it seems likely that on the equatorial plane they would map to the outer edge of the magnetosphere. The R2 currents, on the other hand, map to the region where the westward ring current circulates around the Earth.

1.5.3 Magnetospheric magnetic field models

Since the magnetic field plays a major role in determining the properties of the geospace plasma, such as its anisotropy, observations made in different regions of space can be compared by mapping them along the geomagnetic field. Hence, knowledge of the structure and dynamics of the geomagnetic field under different conditions of the solar wind is required.

This knowledge can most usefully be expressed in terms of data-based magnetospheric magnetic field models. In such a model, the Earth's internal field, given by the International Geomagnetic Reference Field (IGRF) model, is modified by adding external magnetospheric current systems. The contribution of the internal field is important approximately up to the distance of the geostationary orbit, after which the external field dominates. The magnetic field caused by each major current system is represented mathematically, after which the individual contributions are added up. The representation includes the response of the field to such observable parameters as the orientation of the Earth's dipole axis, interplanetary magnetic field, solar wind pressure and appropriate geophysical indices. Finally, the model is calibrated against an extensive database of averaged magnetic field observations. In addition to the determination of conjugate regions, such as the ionospheric footprints of satellites, a model can help to predict the magnetic field
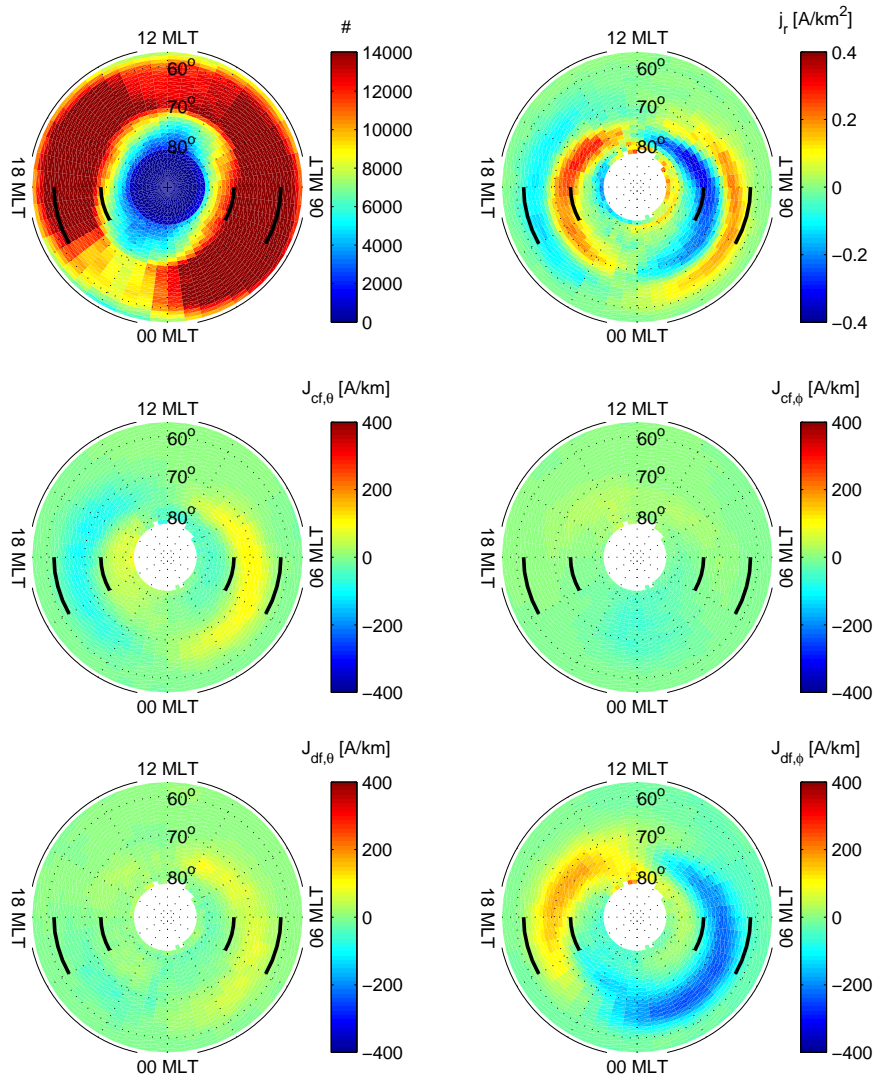
Figure 1.4: Average field-aligned current distribution (top right), the perpendicular currents closing the field-aligned currents (middle) and the perpendicular currents causing the ground-based magnetic signatures (bottom). The average auroral oval, marked by the black arcs between 04–06 and 18–20 MLT, is located between 62°–73° latitude. Figure from PUBL. IV.

expected at a given time and location. The predicted values can then be compared with actual observations, for instance to estimate whether the model is applicable for the event.

Presently, one of the most widely used models is the T89 (Tsyganenko, 1989) model. It only requires the K_p index as input, which makes it easy to use, especially, when processing large amounts of events. The problem of this kind of models, however, is that they may work poorly for specific event studies. Therefore, event-oriented magnetospheric magnetic field models have been developed (e.g., Kubyshkina et al., 1999). An event-oriented model is constructed by modifying an existing model, such as T89. Free parameters are determined for each current system, which are then varied in order to get the best fit between the model and all available observations during the event.

1.5.4   Ionosphere as a monitor

The spacecraft currently scattered across the magnetosphere do not come close to covering the entire region. Moreover, the view one satellite has of its surroundings is very limited, and without additional information, it is often difficult to distinguish whether an observed transient signature is caused by a temporal change in the ambient conditions or by a structure passing the spacecraft. The velocity, size and lifetime of such a structure are impossible determine, as is the spatial extent of the temporal change. With a cluster of several spacecraft (e.g., the Cluster mission, Sect. 3.2.1), the situation is somewhat improved and the temporal and spatial changes can be told apart. Moreover, with some assumptions about the shape of the passing structure, its velocity and size in the direction of the motion can be calculated. The size perpendicular to the motion, on the other hand, can only be estimated if it happens to be comparable to the distances between the spacecraft. The same applies to the spatial extent of the temporal change. However, the lifetime of the moving structure is still likely to remain unknown.

Ionospheric observations can be utilised to place spacecraft observations in context within the large scale magnetospheric structures and to distinguish between spatial and temporal gradients in the satellite data. Due to its smaller size and proximity to the Earth, monitoring the ionosphere is much easier and can be done using, for instance, ground-based networks or satellite imagers. Apart from plasmoids, magnetospheric field lines are generally connected to the ionosphere, which can thus be regarded as a monitor of the much larger magnetosphere, provided that the implications of the observed signatures in terms of magnetospheric processes are understood.

The interpretation of ionospheric signatures in terms of magnetospheric phenomena is quite challenging, partly because the proportions of the magnetosphere become severely distorted when projected on the ionosphere along the geomag-

netic field lines. The projection of the relatively small inner magnetosphere covers the unproportionately large region between the auroral ovals, while the entire plasma sheet, where the most interesting dynamics occur, is squeezed into the narrow ovals. While the GSM y-direction is still relatively well represented in the ovals, the x-direction is severely contracted. Moreover, information between the magnetosphere and the ionosphere is carried by Alfvén waves travelling at the Alfvén speed $V_A = B/\sqrt{\mu_0 \rho}$, which is about 0.1–1 R_E/s. This means that, depending on the location of the magnetospheric source and the ambient conditions along the signal path, it takes from seconds to minutes for the signal to reach the ionosphere. This time delay can cause further ambiguity, when trying to couple magnetospheric observations with their ionospheric counterparts.

Chapter 2

Geomagnetic activity

Variations in the geomagnetic field caused by sources external to the Earth are generally referred to as geomagnetic activity, and include, for instance, geomagnetic storms, substorms and aurora. The practical impact of this activity on human technology is termed space weather. The long term variability in the geomagnetic activity has several sources. For instance, the variability of the Sun itself that is reflected on the solar wind causes the 11- and 22-year solar cycles, while the rotation of the Sun around its axis produces a periodicity of 27 days. The level of geomagnetic activity is measured using different activity indices, such as D_{st}, K_p and AE, most of which are derived from ground-based magnetic field measurements. The indices are also often used to bin observation with respect to the level of geomagnetic activity.

2.1 Magnetic indices

Depending on the latitudinal locations of the magnetometer stations from which the magnetic index is derived, different indices are suitable for describing different aspects of geomagnetic activity. For instance, the low-latitude D_{st} index is mainly affected by the ring current, and can therefore be used to monitor magnetic storms, while the AE index obtained from the high-latitude auroral region describes substorm activity. The mid-latitude K_p index, on the other hand, is affected by both current systems, and is therefore a more general indicator of the global activity level.

2.1.1 D_{st} index

The D_{st} index (Sugiura, 1964) is derived from the horizontal component of the magnetic field measured by four ground-based low-latitude magnetometer stations

distributed roughly evenly around the Earth. The baseline, including the secular variation, as a function of UT hour is computed as the annual mean of the five quietest days of each month, and the solar quiet daily variation as a function of UT hour is computed as the mean of the five quietest days of the month. Secular variation refers to the slow change of the Earth's magnetic field on time scales ranging from year to millennia, and the geomagnetic solar quiet daily variation field is a regular daily variation caused by ionospheric and magnetospheric current systems. For each station, the baseline and the secular variation are subtracted from the observed magnetic field and D_{st} is computed as the average of the four stations weighted inversely by the cosine of the dipole latitude of the station.

The D_{st} index represents the axially symmetric disturbance magnetic field at the dipole equator on the Earth's surface. Major disturbances in D_{st} are negative, corresponding to decreases in the geomagnetic field. These decreases are produced mainly by the ring current, but also the cross-tail current makes a small contribution. Positive variations in D_{st} are mostly caused by the compression of the magnetosphere due to solar wind pressure increases.

2.1.2 K_p index

The K_p index (Bartels et al., 1939) is obtained from 13 mid-latitude geomagnetic observatories, eleven of which are located in the northern and two in the southern hemisphere. For each 3-hour interval, the local disturbance levels at each station are determined by taking the largest excursion in the two horizontal components with the effects of annual and daily variations eliminated. The K_p index is obtained as the mean value of these disturbances, placed on a scale ranging from 0 to 9. Variations in K_p are difficult to interpret physically since, depending on the level of magnetic activity, the stations are under the influence of different current systems.

2.1.3 AE index

The auroral electrojet (AE) indices (Davis and Sugiura, 1966) are derived as one-minute values from the horizontal component of the magnetic field measured by 10–13 ground-based magnetometer stations located along the auroral zone of the northern hemisphere. A monthly baseline value for each station is calculated by averaging all data from the station on the five internationally quietest days. The baselines are subtracted from the observed data, and for each given UT time, the largest and smallest of the resulting values among all stations are selected. The largest value is called the AU index, the smallest the AL index, and the difference $AU - AL$ the AE index.

The AU and AL indices are intended to describe the strongest eastward and westward current, respectively, while the general electrojet activity is represented by the AE index. However, the auroral oval can move considerably in latitude and, hence, the electrojets are not well covered during very quiet and very active conditions.

The IE index is a local equivalent of AE, determined from IMAGE magnetometer network measurements (Sect. 3.1.1), and is provided as minute values. Similarly, the IL and IU indices are the local equivalents of the global AL and AU indices. These indices have been utilised in PUBL. V.

2.2 Substorm

Originally, Akasofu (1964) described the substorm in terms of auroral dynamics, and this ionospheric manifestation of the phenomenon is often referred to as the auroral substorm. The substorm, however, is a process encompasing the entire solar wind-magnetosphere-ionosphere system. Substorms typically last 2–3 hours and occur at a rate of about four per day (Borovsky et al., 1993). During intense solar wind driving, however, they take place more frequently and are more intense, while during weak solar wind driving, long quiet periods can occur.

2.2.1 Auroral substorm

The auroral substorm is generally divided into three main phases: the growth phase, the expansion phase, and the recovery phase (Akasofu, 1964; McPherron, 1970). In addition to optical signatures, these phases can also be recognized from ground-based magnetometer observations, such as the AE index.

During the growth phase, the auroral oval moves equatorward, and particularly on the nightside, east-west oriented auroral arcs drifting slowly equatorward can be observed. The AE index starts to grow, indicating enhanced magnetospheric and ionospheric convection.

The beginning of the substorm expansion phase is referred to as the substorm onset. The onset is signified by an auroral breakup, during which typically the equatorwardmost of the equatorward drifting arcs intensifies and forms the so-called auroral bulge. While several brightenings can occur already during the growth phase, the onset is the intensification leading to the full-scale dynamics. The point where the activation is first observed is termed the onset location. Typically, the location varies between about 20–01 MLT and $62°$ –$72°$ invariant latitude (ILat), with an average at 22.6 MLT and $66.8°$ ILat (Gjerloev et al., 2007).

During the expansion phase, the auroras expand eastward, westward and poleward from the onset location. The western edge of the expanding bulge is called

the westward travelling surge (WTS). The formation of a channel of intense westward current inside the bulge, called the auroral or substorm electrojet, is associated with magnetic Pi2 pulsations with a period of 40–150 s (Saito, 1969) and a sudden increase of the AE index. During the most intense substorms, the AE index can exceed 1000 nT.

During the recovery phase, the activity shifts to the early morning sector. At the beginning of the recovery phase, the auroral oval is very wide, and often splits to form a double-oval (Elphinstone et al., 1993). The poleward edge of the oval starts to retreat equatorward. Eastward drifting auroral structures, called omega bands due to their shape, are occasionally observed. The auroral electrojet decays, causing the AE index to slowly decrease.

Typically, the growth phase continues for less than an hour, the expansion phase for about 30 minutes, and the recovery phase for 1–2 hours, amounting to a total substorm duration of about 2–3 hours. However, individual substorms often differ considerably from each other. Particularly during storm periods, the growth phase of a new substorm may begin before the recovery phase of the previous one has ended. The durations of the different phases vary considerably, and the end of the recovery phase is not always unambiguous. It is also common for several activations to occur during one substorm. During the growth phase, smaller activations that do not lead to the expansion phase may take place. These activations, called pseudobreakups, are localized and only last for a few tens of minutes (e.g., Koskinen et al., 1993).

2.2.2 Magnetospheric substorm

The solar wind energy, momentum and plasma enter the magnetosphere via magnetic reconnection and viscous interactions (Dungey, 1961; Axford and Hines, 1961). When the energy input is small, the energy is dissipated in the ionosphere and the magnetic flux opened by the dayside reconnection process is closed by the reconnection process in the distant magnetotail at about 100–200 R_E from the Earth. During enhanced energy input, however, the dayside and nightside reconnection rates are rarely balanced, although such Steady Magnetospheric Convection (SMC) events, lasting up to ten hours, have been observed (Sergeev et al., 1996). More often, enhanced energy input from the solar wind to the magnetosphere leads to a loading-unloading sequence called a magnetospheric substorm. For instance, Kamide et al. (1977) showed that substorms occur with a 100% probability whenever the southward component of the 1-hour averaged IMF exceeds -3 nT.

Enhancement of the energy input from the solar wind to the magnetosphere, often caused by the southward turning of the IMF, initiates the substorm growth phase, during which energy is loaded into the magnetotail. The resulting increase

of the magnetic flux in the tail lobes, which can be observed as the equatorward motion of the auroral oval in the ionosphere, streches the tail and consequently enhances the magnetospheric current systems and compresses the plasma sheet, leading to the formation of a thin (down to 0.1 R_E), intense current sheet between about 6–15 R_E tailward from the Earth (Sergeev et al., 1990).

During the substorm expansion phase, the energy stored in the tail is unloaded. According to satellite observations, the field lines of the inner magnetosphere relax from their streched configuration to a more dipolar configuration. During this dipolarisation process, the plasma sheet expands, and fast earthward and tailward plasma sheet plasma flows and particle injections at the geostationary orbit are observed. A portion of the plasma sheet magnetic field and plasma is detached from the geomagnetic field, and this plasmoid is ejected downstream to the solar wind. The tail field reconfiguration is also associated with strong field-aligned currents between the magnetosphere and the ionosphere, which in part contribute to the energy dissipation in the ionosphere.

A part of the cross-tail current is disrupted, and it closes through the ionosphere, forming a current loop called the substorm current wedge (SCW, McPherron et al., 1973). On the eastern edge of the substorm current wedge, the cross-tail current is diverted to the ionosphere via downward field-aligned current. In the ionosphere, the current flows westward, forming the substorm electrojet, and returns to the magnetosphere via the upward field-aligned current on the western edge of the substorm current wedge. The westward travelling surge is then the auroral signature of the upward field-aligned current. According to recent observations, however, the upward current of the WTS does not wholly originate from the eastern edge of the SCW, but is partly closed by local downward field-aligned currents (Marklund et al., 1998; Amm and Fujii, 2008).

At present, there are two main competing model to explain the observations. According to the near-Earth neutral line model (Baker et al., 1996), the thin current sheet becomes unstable, possibly due to the tearing mode instability, leading to the formation of a reconnection region at about 20–30 R_E distance from the Earth. Because the reconnection rate is proportional to the Alfvén speed of the inflowing plasma, the process is relatively slow as long as it remains on the closed magnetic field lines where plasma is abundant. After the last closed field line is reached, the reconnection rate increases abruptly, which is often interpreted as the onset of the expansion phase. The poleward expansion of aurora in the ionosphere then results from the sudden decrease of the open magnetic flux in the tail lobes. Dipolarisation and fast plasma sheet flows are explained by the outflow from the reconnection region, while the plasmoid is formed between the near-Earth neutral line and the distant neutral line, and released when reconnection severs the last closed field lines and proceeds to the open field lines. The SCW is also predicted by the model. The plasma flows earthward from the X-line in a narrow channel.

Because the channel is limited in the cross-tail direction, the flow shear between the fast flow and the ambient earthward plasma flow within the plasma sheet creates a pair of field-aligned current sheets with upward field-aligned current on the duskside and downward field-aligned current on the dawnside of the channel. When the flow reaches the strong field in the inner magnetosphere, it slows down and splits in two in order to circulate around the Earth. Furthermore, the reconnection process is associated with rapid and significant conversion of magnetic energy in the magnetotail lobes to particle kinetic energy and heat in the plasma sheet.

According to the current disruption model (CD, e.g., Lui et al., 2008), on the other hand, current disruption within about 15 R_E from the Earth causes the magnetic field to relax to a more dipolar configuration, which gives rise to dipolarisation and fast flows. The current disruption process instigates further disruption in the adjacent regions by thinning the plasma sheet and enhancing the cross-tail current, which allows the current disruption to occur progressively down the magnetotail. Later, magnetic reconnection may develop at one of these current disruption sites.

When the extra energy stored during the growth phase has been exhausted, or the energy input from the solar wind decreases, the magnetosphere starts to return to its quiet state. During this recovery phase, the magnetotail stretches back to its original form after the dipolarisation overshoot of the expansion phase. This can be observed in the ionosphere as the equatorward retreat of the poleward edge of the oval, caused by the restoration of magnetic flux to the tail lobes. According to the near-Earth neutral line model, the near-Earth neutral line propagates down the tail to replace the distant neutral line that was lost at the release of the plasmoid.

The size of the substorm is closely related to the energy input from the solar wind to the magnetosphere. If the IMF turns northward during the growth phase or near the onset, the ensuing substorm tends to be small, whereas continuous energy input throughout the entire expansion phase is likely to produce stronger activity (Kallio et al., 2000).

During pseudobreakups, the expansion phase processes, such as the current disruption, substorm current wedge, and dipolarisation occur as localised versions of the corresponding global scale substorm phenomena (Pulkkinen, 1996; Aikio et al., 1999). Suggestions for the conditions that prevent the pseudobreakups from evolving into fully fledged substorms include too slow or too transient energy input from the solar wind to the magnetosphere, insufficient storage of energy in the magnetotail (Nakamura et al., 1994; Amm et al., 2001) and ionospheric conductivity, which is not high enough to close the substorm current wedge (Koskinen et al., 1993).

2.3 Magnetic storm

The magnetic storm is a geomagnetically disturbed period lasting from several hours to several days, characterized by a decrease of the D_{st} index (Chapman and Bartels, 1940). Substorms require a period of enhanced energy input from about 30 minutes to an hour. If the energy input continues significantly longer (over three hours) a magnetic storm develops (Gonzalez et al., 1994). Therefore, coherent solar wind structures, such as coronal mass ejections (CME) and high speed solar wind streams, are effective drivers of magnetic storms. While substorms can occur without magnetic storms, all storms include also substorm activity.

The magnetic storm begins with a sudden commencement (SSC) after which it can be divided into the initial phase, the main phase and the recovery phase, identifiably from a time series of the D_{st} index. The initial phase is characterized by a positive excursion of the D_{st} index, caused by the compression of the dayside magnetopause as the CME or other structure hits it (Chapman and Ferraro, 1931). During the main phase, the D_{st} index decreases rapidly, the auroral ovals move equatorward, and the occurence rate of substorms increases. The magnitude of the decrease in D_{st} represents the severity of the disturbance. During the recovery phase, the D_{st} index slowly recovers and the auroral ovals retreat poleward to their nominal locations. The decrease of the D_{st} index during the main phase is caused by the increase of the ring current. Particularly during substorm expansion phases, charged particles are injected into the inner magnetosphere, where they become trapped by the magnetic bottle. When the energy input from the solar wind decreases, and new particles are no longer injected, the current slowly begins to decrease.

2.4 Space weather

The term space weather refers to conditions on the Sun, in the solar wind, magnetosphere, ionosphere, and thermosphere that can be harmful to technological systems or human health in space and on ground. Solar irradiation, energetic particle fluxes from the Sun, and the solar wind with its various structures all drive geomagnetic activity and are thus potential sources for space weather effects, such as disruption of satellite operations, communications, navigation and electric power distribution grids on ground.

The time scales of space weather processes vary from the 11 year solar cycle and longer (long-term solar activity variations) to 27 days (recurrent solar activity), days (magnetic storms) and hours (substorms). The lead time obtained by prediction, on the other hand, depends on how long before reaching the Earth the event can be observed. Electromagnetic radiation travels the distance between

the Sun and the Earth in about 8 minutes, while energetic particles, after their release from the solar surface or an interplanetary shock front, reach the Earth within about 20 minutes. The solar wind travel time from the Sun to the Earth is of the order of 80 hours, and from the solar wind monitores, located at the first Lagrangian point (L1), about an hour (Pulkkinen, 2007).

The final goal of space weather research is to be able to produce reliable forecasts and nowcasts of the state of the space environment and its effects. In order to reach this goal, it is first essential to learn to quantitatively predict the state of the magnetosphere and the ionosphere from the solar wind observations.

Chapter 3

Measurements

In this chapter, the instruments that have produced the data utilised in PUBL. I–V are briefly described.

3.1 Ionosphere

3.1.1 MIRACLE/IMAGE

The Magnetometers - Ionospheric Radars - Allsky Cameras Large Experiment (MIRACLE, [04]) is a two-dimensional ground-based instrument network comprising magnetometers, radars and all-sky cameras. The network covers an area from subauroral to polar cap latitudes over a longitude range of about two hours of local time (Fig. 3.1) and is maintained and operated as international collaboration under the leadership of the Finnish Meteorological Institute.

The International Monitor for Auroral Geomagnetic Effects (IMAGE, [05]) magnetometer network of MIRACLE currently consists of 30 magnetometer stations maintained by 10 institutes from Estonia, Finland, Germany, Norway, Poland, Russia and Sweden. The network was designed mainly for two kinds of studies: while the extensive coverage from 58° to 79° geographic latitude (54°–75° CGM latitude) favours electrojet studies, the 10 second temporal resolution and the unique mesoscale (10–1000 km) spatial resolution are suitable for studies of moving two-dimensional current systems. Particularly, the latitudinally extended TAR-NAL chain is suitable for monitoring electrojet activity. The network utilises fluxgate magnetometers (e.g., Campbell, 1997) to measure the three components of the magnetic field. The disturbance magnetic field is obtained by subtracting a baseline value from the measured field. The average magnetic field during a quiet period close to the event is generally used as the baseline. IMAGE data have been used in PUBL. I–III and V.
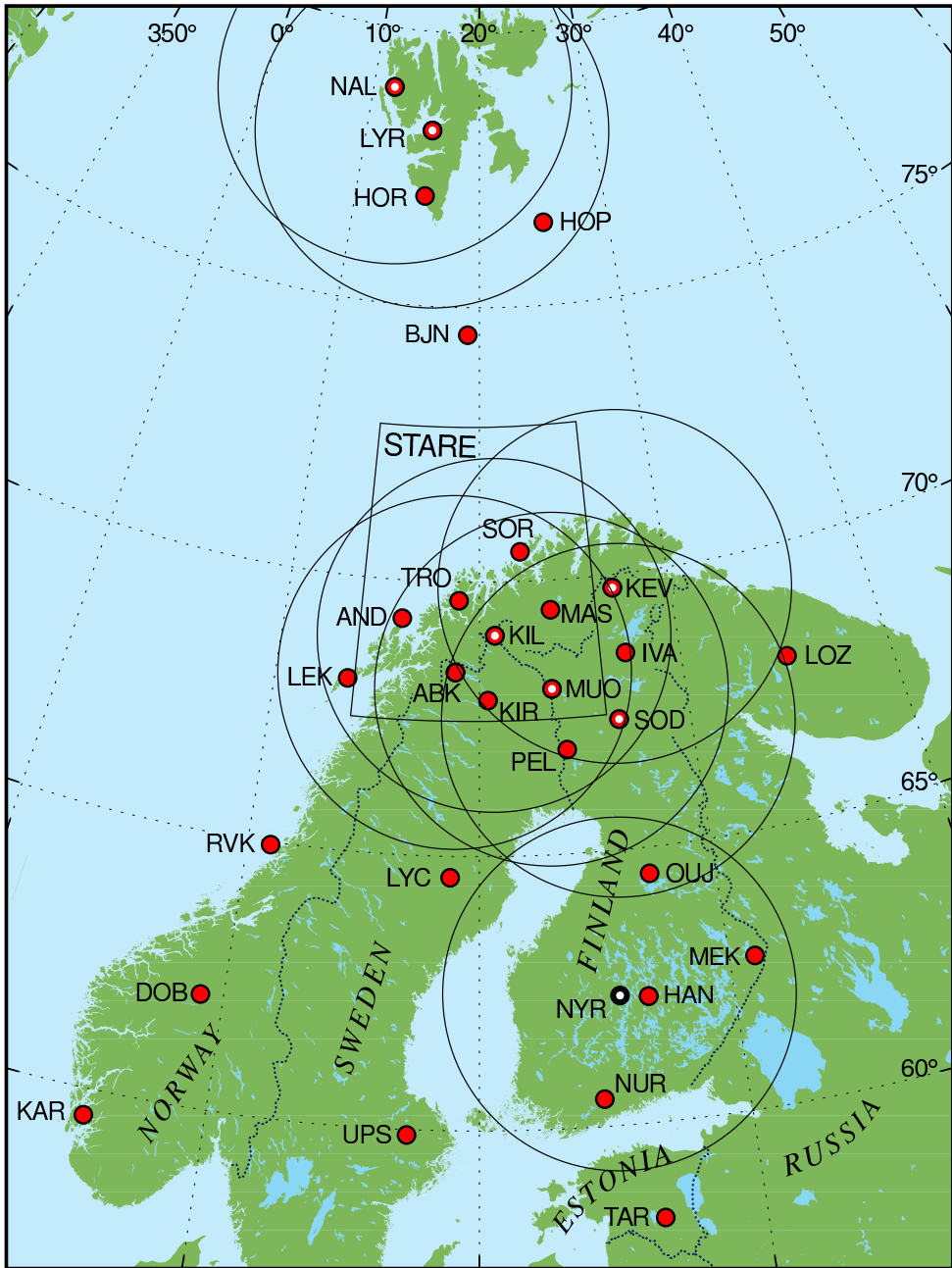
Figure 3.1: Magnetometers (IMAGE) and all-sky cameras of the MIRACLE network. Illustration by Lasse Häkkinen.

3.1.2 CHAMP

CHAMP (CHAllenging Minisatellite Payload, [06]) is a European small satellite mission. It was launched on 15 July 2000 into an almost circular, near polar ($i = 87^o$) orbit with an initial altitude of 454 km, but due to atmospheric drag, the altitude had decreased to about 350 km by the end of 2005. CHAMP has a period of about 1.5 h, resulting in over 15 revolutions per day, and all local time sectors are covered in 131 days. The vector magnetic field is measured by the fluxgate magnetometer on board.

The 1 Hz data, which have been used in PUBL. I, II and IV, correspond to about 7.5 km distance between successive measurement. The variation magnetic field is obtained by subtracting from the measurements the CO2 main field model (Holme et al., 2003), employed up to degree and order 14, and the ring current effect (D_{st}-correction) using the external set of coefficients of the same model.

3.1.3 EISCAT

The European Incoherent SCATter (EISCAT, [07]) Scientific Association is an international research organisation operating three incoherent scatter radar systems in Northern Fennoscandia and Svalbard. It is funded and operated by the research councils of Norway, Sweden, Finland, Japan, China, the United Kingdom and Germany. The EISCAT Svalbard Radar (ESR) utilises 500 MHz Ultra High Frequence (UHF) radio waves. The mainland radars comprise a transmitter site in Tromsø, Norway, consisting of a 931 MHz UHF system and a 224 MHz Very High Frequency (VHF) system, and additional UHF receivers located in Sodankylä, Finland, and Kiruna, Sweden.

The radar transmits a high power electromagnetic wave of about 1 MW to the ionosphere, where it is scattered by electron density fluctuations in the radar beam. The basic microscopic mechanism is Thomson scattering from free electrons, which, on the other hand, follow the thermal fluctuations of the heavier ions. The scattered signal is detected by a large antenna and a sensitive receiver system. Incoherent scatter is very weak: the received power is only about 10^{-16} MW, but with advanced analysis methods (e.g., Nygrén, 1996), electron density, ion drift velocity component, and electron and ion temperatures as a function of altitude up to about 1000 km can be extracted.

In PUBL. II, the Hall-to-Pedersen conductance ratio measured by the EISCAT mainland radar was utilised. Using the MSIS-86 model (Hedin, 1987) for the ion-neutral collision frequency, the Hall and Pedersen conductivities were calculated from the electron density, and the conductances were obtained by height-integration.

3.1.4 IMAGE satellite

On 25 March 2000, the National Aeronautics and Space Administration (NASA) mission Imager for Magnetopause-to-Aurora Global Exploration (IMAGE, [08]) satellite was launched into an elliptical polar orbit (inclination 90°) with an apogee altitude of 7.2 R_E, a perigee altitude of 1000 km, and a period of 14.2 hours. The mission ended on 18 December 2005.

The Far Ultraviolet (FUV) instrument on-board IMAGE employed three detectors, one of which was the Wideband Imaging Camera (WIC) to image auroral emissions in the wavelength range 140–190 nm with a temporal resolution of about 2 minutes. These data are employed in PUBL. III.

3.2 Magnetosphere

3.2.1 Cluster

The European Space Agency (ESA) and NASA Cluster mission [09] was launched in two phases on 16 July and on 19 August 2000 into an elliptical polar orbit with an apogee of 119 000 km (∼19 RE), a perigee of 19 000 km (∼3 RE) and a period of 57 hours. Cluster consists of four identical spacecraft that fly in a tetrahedral configuration. The separation distances between the spacecraft vary between 600 km (0.1 R_E) and 20 000 km (3 R_E). The aim of the mission is to investigate in-situ the small-scale structure of the Earth's magnetosphere. The four spacecraft permit the study of three-dimensional and time-varying phenomena and make it possible to distinguish between spatial and temporal variations. The simultaneous four-point measurements also allow differential plasma quantities to be derived for the first time. For example, current density is derived from the magnetic field measurements using Ampère's law. The mission will continue at least until December 2009.

Each of the four spacecraft carries an identical set of 11 instruments to investigate charged particles, electric and magnetic fields. Data from two of them, the Fluxgate Magnetometer (FGM, Balogh et al., 2001), with a temporal resolution up to 67 samples per second, and the Hot Ion Analyser (HIA) of the Cluster Ion Spectrometry experiment (CIS, Rème et al., 2001) have been utilised in PUBL. III and V.

The CIS/HIA instrument determines the ion velocity distribution function and its moments during each four second spin of the spacecraft for particles with energies per charge of about 5 eV/e–32 keV/e. The energy range from a few eV to a few keV is sometimes referred to as the "hot plasma" regime. Since the analyser does not distinguish between particles of different masses, the velocity

space distribution function is computed from the energy per charge distribution by assuming that the particles are protons.

Moments are constructed from the velocity distribution function $f(\mathbf{v})$ with the maximum time resolution of one spin period or four seconds. They are defined as

$$M_n = \int f(\mathbf{v})\mathbf{v}^n d\mathbf{v}. \tag{3.1}$$

The moments include the number density N ($n = 0$), the number flux density vector $N\mathbf{V}$ ($n = 1$), the momentum flux density tensor $\mathbf{\Pi}$ ($n = 2$) and the energy flux density vector $\mathbf{Q}$ ($n = 3$). From these can be derived the average velocity $\mathbf{V} = (N\mathbf{V})/N$ and the pressure tensor $\mathbf{P} = \mathbf{\Pi} - m_p N\mathbf{V}\mathbf{V}$. Using the definition $\mathbf{P} = Nk_B\mathbf{T}$, the pressure tensor can be converted into a temperature tensor. Scalar pressures and temperatures can be obtained from the trace of the associated tensors: $P = Tr(\mathbf{P})/3$, $T = Tr(\mathbf{T})/3 = P/(Nk_B)$. Besides instrument sensitivity and calibration, the accuracy of computed moments is mainly affected by the finite energy and angle resolution, and by the finite energy range.

3.3 Solar wind

3.3.1 ACE

The NASA mission Advanced Composition Explorer (ACE, [10]) was launched on 25 August 1997. ACE orbits the L1 Lagrange point, located about 0.01 AU from Earth on the Sun-Earth line. The orbit ranges between 220 $R_E < x_{GSE} <$ 250 R_E, -40 $R_E < y_{GSE} < 40$ R_E and -24 $R_E < z_{GSE} < 24$ R_E. The interplanetary magnetic field is measured by the Magnetometer (MAG) instrument on board ACE and the Solar Wind Electron, Proton, and Alpha Monitor (SWEPAM) provides data on the solar wind density and velocity.

3.3.2 Wind

Wind [11] was launched November 1, 1994, as part of NASA's contribution to the International Solar Terrestrial Program. Since mid-2004, it has been in an L1 orbit with -100 $R_E < y_{GSE} < 100$ R_E. Earlier phases include an interval spanning the last third of 2000 through mid 2002 with -200 $R_E < y_{GSE} < 200$ R_E and an interval in late 2003 and early 2004 in orbit about the Lagrange point on the anti-sunward side of Earth. The interplanetary magnetic field is measured by the Magnetic Fields Investigation (MFI) instrument and the Solar Wind Experiment (SWE) instrument provides data on the solar wind density and velocity.

The interplanetary magnetic field and solar wind proton density and flow speed measurements utilised in PUBL. II and IV were obtained from the GSFC/SPDF OMNIWeb interface at [12]. The ACE and Wind data accessible through the interface were 1-min-averaged field and plasma data sets shifted to the Earth's bow shock nose. Since the location of observation may be an hour upstream of the magnetosphere, and several tens of R_E removed from the Sun-Earth line, it is useful for solar wind-magnetosphere coupling studies to time-shift the solar wind data to a point closer to the magnetosphere, such as the bow shock nose determined from a model. The time shifting is based on the assumption that solar wind magnetic field values observed by a spacecraft at a given time and place lie on a planar surface convecting with the solar wind, and that the same values will be seen at a different place at the time that this phase front sweeps over that location. One of the primary shortcomings of time shifting are out-of-sequence arrivals due to speed gradients or to variously oriented phase planes. The approach was to accept all shifted data as belonging to the newly assigned time tags.

Chapter 4

Ionospheric currents from magnetic measurements

In this Chapter, determination of ionospheric currents in spherical coordinates (r,θ,ϕ) from magnetic field measurements (B_r,B_θ,B_ϕ) using the Spherical Elementary Current System (SECS) method is discussed. Since this requires some assumptions about the geometry of the currents, the thin-sheet approximation and the assumption of vanishing parallel electric field (Sect. 1.4.3) is used. Hence, the expressions below and above the ionosphere refer to altitudes below and above 100 km, respectively. This is feasible, since in regard to the magnetic field at about 100 km distance or more, the ionospheric currents effectively look like a surface current distribution. Furthermore, the geomagnetic field lines are assumed to be radial, that is, $\hat{e}_{||}$ is replaced by $-\hat{e}_r$ in the northern hemisphere and by $\hat{e}_r$ in the southern hemisphere. Moreover, the current distribution is assumed to be stationary, so that the currents are given by Ampère's law (Eq. 1.4).

During geomagnetically disturbed conditions, the time-varying magnetic field of the ionospheric and magnetospheric currents induces electric currents in the conducting ground, which in turn contribute to the disturbance magnetic field. For instance, during highly dynamic substorm onset periods, about 40% of the IL index can be of internal origin, but during quiet times, the contribution is only about 10–20% (Tanskanen et al., 2001). These ground-induced currents could be modeled using the SECS method by placing a second current layer below the surface of the Earth and expressing the current density on it as a superposition of the divergence-free SECSs (Pulkkinen et al., 2003), but in this study this effect is ignored.

4.1 Spherical Elementary Current System (SECS) method

The perpendicular ionospheric current density $\mathbf{J}$, like any vector field, can be divided into divergence-free (df) and curl-free (cf) components

$$\mathbf{J}(\theta, \phi) = \mathbf{J}_{cf}(\theta, \phi) + \mathbf{J}_{df}(\theta, \phi) \qquad (4.1)$$

$$\nabla \cdot \mathbf{J}_{df} = 0 \qquad (4.2)$$

$$(\nabla \times \mathbf{J}_{cf})_r = 0. \qquad (4.3)$$

According to current continuity (Eq. 1.14), field-aligned currents are related to the divergence of the curl-free component, which thereby closes them. If only sub-areas of a sphere are considered, an additional Laplace component of the current density ($\mathbf{J}_L$) may exist, for which $\nabla \cdot \mathbf{J}_L = 0$ and $(\nabla \times \mathbf{J}_L)_r = 0$. This component, which can be written as $\mathbf{J}_L = \nabla \Phi$, where Φ must fulfil the Laplace equation $\nabla^2 \Phi = 0$, is caused by curls and divergences of $\mathbf{J}$ located outside the observed region.

4.1.1 2-D SECS

The 2-D Spherical Elementary Current System (SECS) method (Amm, 1997; Amm and Viljanen, 1999) is a technique with which $\mathbf{J}_{df}$, $\mathbf{J}_{cf}$ and j_r can be determined from vector magnetic field measurements. According to this method, the perpendicular ionospheric current density is expressed as a superposition of curl-free and divergence-free spherical elementary current systems, with radial field-aligned currents associated with the divergence of the curl-free SECSs (Fig. 4.1). The locations of the SECS poles are distributed over the region of interest, and each SECS may have a different amplitude. The magnetic fields of the SECSs can be expressed analytically, which makes it possible to determine the ionospheric current density, i.e., the SECS amplitudes, by optimally matching the measured disturbance magnetic field to the superposed magnetic field of the SECSs. Either ground-based or satellite-based data can be used separately or, if available, a combination of both. However, while the divergence-free SECS causes a magnetic field both below and above the ionosphere, the magnetic field of the combined curl-free SECS and field-aligned currents is confined to the region above the ionosphere (Fukushima, 1976). Thus, only the divergence-free component can be determined from ground-based magnetic field data, while the full 3-D distribution, including $\mathbf{J}_{df}$, $\mathbf{J}_{cf}$, and j_r, can be derived from satellite-based measurements. While deviation of the geomagnetic field from the radial direction causes the combined magnetic field of $\mathbf{J}_{cf}$ and $j_{\parallel}$ to leak below the ionosphere, Untiedt and Baumjohann (1993) have shown that in the region covered by the IMAGE

$\vartheta'=0$ (pole)

Curl-free elementary system
(with associated FACs)

Divergence-free elementary system
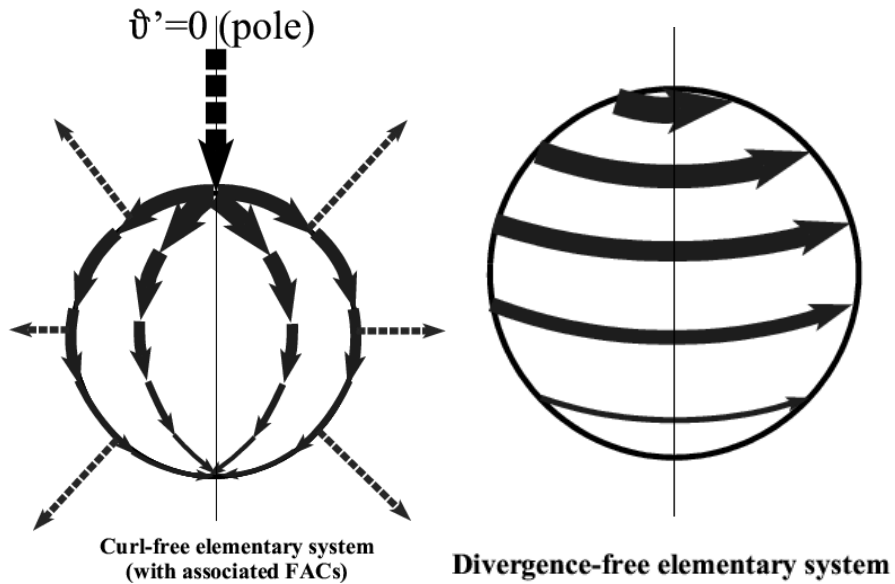
Figure 4.1: *Left:* The curl free 2-D SECS with associated field-aligned currents. *Right:* The divergence-free 2-D SECS. Illustration by Olaf Amm.

magnetometer network, for instance, where the geomagnetic field lines are on average inclined from the radial direction by 13°, the magnetic field of $\mathbf{J}_{cf}$ and $j_{||}$ is still hardly observable on the ground.

The locations of the SECS poles can be chosen freely to best accommodate the location and density of the available measurement points. Any curls or divergences outside the covered region, which is often extended outside the measurement region, are thus assumed to vanish. Due to the strong attenuation of their magnetic field, current structures with scale lengths smaller than about 50 km will not be discernible on the ground. Therefore, ground-based magnetic field data are suitable only for the determination of current systems at scale lengths larger than 50 km. Furthermore, part of the smaller-scale (<10 km) current systems can close at higher altitudes than the larger-scale ones (e.g., Brekke, 1997). Although contribution from such smaller-scale structures can be present in satellite-based magnetic field data, part of these current systems do not reach the 100 km altitude, and therefore cannot be represented by the thin-sheet current system. Placing the SECSs about 50 km apart assures that the current structures at this and larger scales will be optimally matched to the magnetic field data.

4.1.2   1-D SECS

If magnetic data are only available along a single line, such as a ground-based magnetometer chain or the track of a low-orbit satellite, the 2-D SECS method cannot be used. Instead, assuming that the perpendicular current distribution is one-dimensional, i.e., independent of the ϕ coordinate, the 1-D SECS method (Vanhamäki et al., 2003) can be applied. With satellite-based data, the additional assumption of stationary current distribution during the overflight is required. As any 2-D $\mathbf{J}(\theta, \phi)$ could be expressed as a superposition of 2-D SECSs, similarly any 1-D $\mathbf{J}(\theta)$ can be reproduced using a superposition of 1-D SECSs.

1-D variants of the divergence-free and curl-free SECSs can by derived by placing the poles of infinitely many 2-D SECSs next to each other at a constant θ-coordinate. Then, $\mathbf{J}_{cf}(\theta) = J_\theta(\theta)\hat{\mathbf{e}}_\theta$ and $\mathbf{J}_{df}(\theta) = J_\phi(\theta)\hat{\mathbf{e}}_\phi$. The magnetic field caused by $j_r(r, \theta)$ and $J_\theta(\theta)$ is $\mathbf{B} = B_\phi(r, \theta)\hat{\mathbf{e}}_\phi$ and the magnetic field caused by $J_\phi(\theta)$ is $\mathbf{B} = B_r(r, \theta)\hat{\mathbf{e}}_r + B_\theta(r, \theta)\hat{\mathbf{e}}_\theta$. J_θ and j_r can be computed from B_ϕ using the curl-free 1-D SECSs and similarly, J_ϕ could be determined from B_r and B_θ using the divergence-free 1-D SECSs. However, if only B_r is used instead and B_θ is also computed from it, the difference between the measured and computed B_θ can be used to determine whether the current distribution is 1-D enough that the results given by the method are reliable. In an ideal 1-D case, the computed and measured B_θ would be identical. Furthermore, the 1-D direction does not need to be perpendicular to the satellite track or ground-based magnetometer chain. The optimal 1-D direction can be determined by minimising the difference between the measured and computed B_θ.

The 1-D assumption is mostly applicable to electrojet dominated cases. Although the entire global current system cannot reasonably be expected to be one-dimensional, a local independence of the ϕ coordinate is sufficient, when currents in a limited region are of interest. For instance, currents whose distances from the IMAGE magnetometer region are larger than the diameter of the region ($\sim$2000 km) will hardly be identifiable, for even if their intensity is large, they will create a quasi-homogeneous magnetic field over the whole region. Moreover, such fields are usually quite small, no more than a few tens of nT (Untiedt and Baumjohann, 1993).

The 1-D SECS method for satellite use was developed and tested in PUBL. I and II. Moreover, it was shown that in 1-D cases, the ϕ component of the divergence-free current density determined from ground-based IMAGE magnetometer network data using the 2-D SECS method corresponds very well with J_ϕ determined from CHAMP satellite data using the 1-D SECS method.

The 1-D assumption also produces other interesting traits. If inductive effects are assumed negligible, then, according to $(\nabla \times \mathbf{E}_\perp(\theta, \phi))_r = 0$ (Eq. 1.15), in a 1-D case $E_\phi(\theta) = const./\sin(\theta)$. Since E_ϕ must remain finite also near the

poles, the constant must be zero. Thus, $\mathbf{E}_\perp(\theta) = E_\theta(\theta)$, $\mathbf{J}_P = \mathbf{J}_{cf} = J_\theta(\theta)\hat{\mathbf{e}}_\theta$, $\mathbf{J}_H = \mathbf{J}_{df} = J_\phi(\theta)\hat{\mathbf{e}}_\phi$, and $\alpha(\theta) = -J_\phi(\theta)/J_\theta(\theta)$. This means that the Hall and Pedersen conductivities can only vary in the direction of $\mathbf{E}_\perp$ (Eq. 4.7 and 4.10), which is anyway required in a 1-D case, and that α can be estimated from currents or magnetic field data only, as was done in PUBL. II.

4.2 Ionospheric equivalent currents

$\mathbf{J}_{df}$ causes the same magnetic field below the ionosphere as the original 3-D distribution, consisting of $\mathbf{J}_{df}$, $\mathbf{J}_{cf}$, and j_r (Sect. 4.1.1), and is therefore also called the equivalent current density.

Assuming that

$$\alpha = \Sigma_H(\theta, \phi)/\Sigma_P(\theta, \phi) = const. \tag{4.4}$$
$$(\nabla\Sigma_H(\theta, \phi) \times \mathbf{E}_\perp(\theta, \phi))_r = 0 \tag{4.5}$$

and using Ohm's law (Eq. 1.13), $\mathbf{J}_{df}$ and $\mathbf{J}_{cf}$ can be related to the Hall and Pedersen current densities by

$$[\nabla \times \mathbf{J}(\theta, \phi)]_r = [\nabla \times \mathbf{J}_{df}(\theta, \phi)]_r \tag{4.6}$$
$$= [\nabla \times \mathbf{J}_H(\theta, \phi)]_r + [\nabla\Sigma_P(\theta, \phi) \times \mathbf{E}_\perp(\theta, \phi)]_r \tag{4.7}$$
$$= [\nabla \times \mathbf{J}_H(\theta, \phi)]_r + \frac{1}{\alpha}[\nabla\Sigma_H(\theta, \phi) \times \mathbf{E}_\perp(\theta, \phi)]_r \tag{4.8}$$
$$\Rightarrow \mathbf{J}_{df}(\theta, \phi) = \mathbf{J}_H(\theta, \phi) \tag{4.9}$$
$$\nabla \cdot \mathbf{J}(\theta, \phi) = \nabla \cdot \mathbf{J}_{cf}(\theta, \phi) \tag{4.10}$$
$$= \nabla \cdot \mathbf{J}_P(\theta, \phi) + [\nabla\Sigma_H(\theta, \phi) \times \mathbf{E}_\perp(\theta, \phi)]_r \tag{4.11}$$
$$\Rightarrow \mathbf{J}_{cf}(\theta, \phi) = \mathbf{J}_P(\theta, \phi). \tag{4.12}$$

The assumption of uniform conductances produces the same result, but is more restrictive than Eq. (4.4) and (4.5), which allow conductances to vary in the direction of the elecric field, as long as α is conserved. When Eq. (4.4) and (4.5) are not valid, which, more or less, is always the case in practise, both $\mathbf{J}_P$ and $\mathbf{J}_H$ contribute to $\mathbf{J}_{cf}$, and therefore participate in closing the field-aligned currents. Moreover, both $\mathbf{J}_{df}$ and $\mathbf{J}_{cf}$ contribute to $\mathbf{J}_H$, which flows in the opposite direction from the ionospheric plasma convection.

4.2.1 Estimating field-aligned currents

Often ground-based magnetic field data alone are available, from which only the equivalent current density can be determined. While $\mathbf{J}_{df}$ already provides information on the magnetosphere-ionosphere coupling, it is often more instructive to

study the field-aligned currents, which can also be more easily compared with auroras. Therefore, it is useful to be able to estimate the field-aligned current density from the equivalent current density. Combining Eq. (4.7), (4.11), (1.13) and (1.14) produces such an expression:

$$j_{df,r}(\theta, \phi) = -\frac{1}{\alpha}[\nabla \times \mathbf{J}_{df}(\theta, \phi)]_r \qquad (4.13)$$

(Amm et al., 2002).

To distinguish between the real field-aligned current density j_r and the approximate field-aligned current density computed from $\mathbf{J}_{df}$ by assuming Eq. (4.4) and (4.5), the latter is denoted here by $j_{df,r}$ and called "curl of the equivalent current density". Untiedt and Baumjohann (1993) give some examples of the variety of possible field-aligned current systems corresponding to a channel-like equivalent current density pattern in their Fig. 13 and 14. Although it is clear that in extreme cases Eq. (4.4) and (4.5) would lead to erroneous field-aligned current patterns, it is often the best that can be achieved without additional data sets.

4.2.2 Estimating the Hall-to-Pedersen conductance ratio

Estimation of the field-aligned current density from the equivalent current density also requires an estimate of the Hall-to-Pedersen conductance ratio α. In PUBL. II, a statistical relation between α and J_ϕ was derived:

$$\alpha = \frac{2.07}{\frac{36.54}{|J_\phi[\text{A/km}]|} + 1}, \qquad J_\phi < 0 \qquad (4.14)$$

$$\alpha = \frac{1.73}{\frac{14.79}{|J_\phi[\text{A/km}]|} + 1}, \qquad J_\phi > 0, \qquad (4.15)$$

where $J_\phi < 0$ applies to the westward electrojet on the dawnside and $J_\phi > 0$ to the eastward electrojet on the duskside. Generally, $\alpha \approx 2$ appears to be a good estimate, except for very quiet cases when $|J_\phi|$ is small (<100 A/km). α is also slightly higher on the dawnside than on the duskside, particularly during winter and equinox.

Chapter 5

Ionospheric currents at different spatial scales

The structures displayed by the ionospheric currents vary according to the spatial and temporal scales at which they are being observed. In this Chapter, we discuss the characteristics of the auroral region ionospheric currents, determined from ground-based and low-orbit satellite-based magnetic field data using the spherical elementary currents systems, on two different scales. The statistical dependence of the large-scale (1° in latitude, 0.5 h in MLT) ionospheric currents on solar wind and geomagnetic parameters have been determined from CHAMP measurements. Meso-scale ionosphere-magnetosphere coupling studies, on the other hand, are based on the simultaneous monitoring of the magnetospheric plasma sheet by Cluster and the ionospheric equivalent currents by the IMAGE magnetometers at a spatial resolution up to about 50 km and a temporal resolution of 10 s.

5.1 Statistics of the large-scale ionospheric currents

Since most geomagnetic activity is powered by energy input from the solar wind, detailed understanding of the energy transfer processes and mechanisms under different conditions of the solar wind is needed. As at any given moment, the solar wind interacting with the Earth is described by a simple set of parameters, such as velocity, number density and magnetic field, it is important to know the state of the system as a function of these parameters.

One way to approach the problem is through statistics. Although the statistical representation does not give the exact state of the system at any given moment, it is often the only way to accumulate enough data for a comprehensive picture. Averaging should also smooth out most of the effects produced by other parameters except for those under study.

In PUBL. II and IV, we have investigated statistically the effects of season, geomagnetic activity, and several solar wind parameters on the auroral region ionospheric currents. Unlike in previous studies, all three components ($\mathbf{J}_{df}$,$\mathbf{J}_{cf}$,j_r) are derived on a matching spatial scale containing scale-lengths larger than or equal to 50 km. The magnetic field measured by the satellite at about 400 km altitude also involves contributions from field-aligned current structures with scale lengths smaller than 50 km. The field-aligned current density containing also these smaller scale lengths could be determined, for instance, by applying Ampère's law, as demonstrated in Appendix B of PUBL. I. However, in order to be able to compare all three current density components meaningfully at the 100 km altitude, they must be resolved on a matching spatial scale. As already discussed in Sect. 4.1.1, scale lengths of the divergence-free component smaller than about 50 km cannot be discerned at the distance of about 300 km, and therefore smaller scale lengths should not be present in the curl-free and field-aligned components either. Moreover, as part of the smaller-scale field-aligned current systems can already close above the 100 km altitude (Sect. 4.1.1), Ampère's law can only be used to resolve the field-aligned current density containing smaller scale-lengths at the satellite altitude, not at the 100 km altitude.

5.1.1 Effect of geomagnetic activity

Effects of K_p

The K_p index (Sect. 2.1.2) is a widely used proxy for the level of geomagnetic activity. The T89 magnetospheric magnetic field model (Sect. 1.5.3), for instance, uses K_p as the only input parameter. In PUBL. IV, we studied the intensity and location of auroral ionospheric currents as a function of the K_p index. Fig. 5.1 displays how the the ionospheric current density depends on K_p.

The AACGM latitude of the poleward boundary of the electrojets (the poleward black arc in the figure) as a function of K_p was given by

$$|lat[\text{deg}]| = -0.71 \cdot K_p + 74.3, \tag{5.1}$$

the location of the equatorward boundary (the equatorward black arc) by

$$|lat[\text{deg}]| = -1.4 \cdot K_p + 66.3 \tag{5.2}$$

and the amplitude of the total field-aligned current by

$$|I_r[\text{MA}]| = 1.1 \cdot K_p + 0.6. \tag{5.3}$$

In PUBL. IV, it was also observed that the majority of the Region 1 current on the dawnside and on the duskside was closed by the oppositely directed Region 2 current on the same side. In the winter, for instance, only about 15% of the dawnside current crossed over to the duskside.
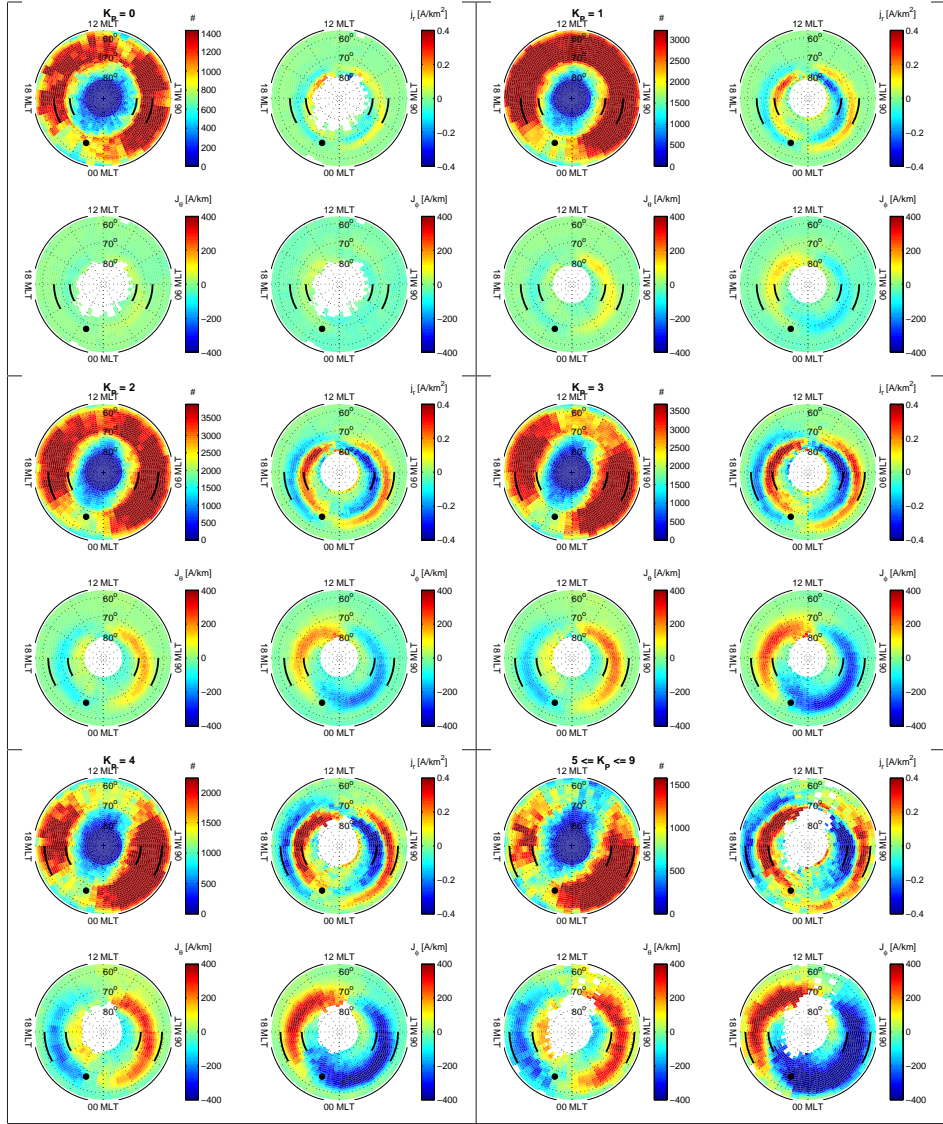
Figure 5.1: Ionospheric current density determined from CHAMP magnetic field data using the 1-D SECS method binned with respect to the K_p index. The panels display the data point distribution (#), field-aligned current density (j_r, positive up), θ component (J_θ, north-south component, positive south), and ϕ component (J_ϕ, east-west component, positive east) of the perpendicular current density. The black dot denotes the average substorm onset location (Sect. 2.2.1). Figure adapted from PUBL. IV.

Substorm electrojet

The westward flowing auroral electrojet is a substorm-related large-scale iono-spheric current system (Sect. 2.2.1), which is often explained in terms of the sub-storm currents wedge (Sect. 2.2.2). While the auroral electrojet is often identified in ground-based magnetic data, the pair of downward and upward field-aligned currents closed in the ionosphere via mainly westward curl-free current, is mag-netically invisible below the ionosphere if the geomagnetic field lines are assumed to be radial. Therefore, the ground-based signature must be caused by westward flowing divergence-free current.

The geometry of the currents agrees with an east-west directed Cowling chan-nel (e.g., Amm, 1997) with downward field-aligned current at its eastward end and upward field-aligned current at its westward end. Inside the channel, the iono-spheric conductances are highly enhanced compared to the ambient ionosphere, and the primary electric field is directed along the channel. If the closure of field-aligned currents via the magnetosphere is inhibited along the channel, the primary Hall currents will build up space charges at the flanks of the channel perpendicu-lar to the electric field. The secondary Pedersen currents caused by this secondary electric field will cancel out the primary Hall currents such that no further space charges are accumulated, and a stationary situation is reached. Hence, the total current, consisting of the primary Pedersen currents and the secondary Hall cur-rents, is directed along the channel. The equivalent current distribution of such a channel consists of westward flow inside the channel and mainly eastward return flow outside the channel.

In panels with $K_p \geq 2$ in Fig. 5.1, the black dot denoting the average substorm onset location lies in the middle of the southern edge of a region where the total current is westward, i.e., J_θ is much smaller than J_ϕ. This region becomes more pronounced with increasing activity. North and west of the onset location there is upward field-aligned current, while north and east of the onset location the field-aligned current is downward. These could be indications of a Cowling channel. However, while the Cowling channel plays an important role for the equatorial electrojet located in the low-latitude region where the geomagnetic field is almost perpendicular, its role in the auroral region, where the geomagnetic field is nearly vertical, has not yet been established (Amm and Fujii, 2008).

5.1.2   Effects of solar wind parameters

IMF

The dependence of large-scale field-aligned currents determined from satellite-based vector magnetic field measurements on solar wind parameters has been

studied extensively. Weimer (2001), for instance, used the vector magnetic field measured by the Dynamics Explorer 2 satellite to derive an empirical model that produces maps of the large-scale field-aligned currents in the high-latitude ionosphere as a function of the IMF, solar wind speed, solar wind density and dipole tilt angle. The model displayed a consistent evolution of the auroral and polar cap current systems as the IMF rotated around the circle. For negative B_z, the model included mainly the R1 and R2 systems, but for positive B_z, an additional current system appeared poleward of the R1 system. This R0 or NBZ system consisted of two regions of upward and downward field-aligned current with a polarity opposite to the surrounding R1 currents. For positive B_y, the upward R1 current on the duskside wrapped through noon to become the dawnside R0 current, while the downward R1 current on the dawnside continued into the R2 current on the dawnside. The upward R0/R1 current encircled a small region of downward current, which appeared to be a remnant of the other pair in the NBZ system. Doubling the IMF magnitude intensified the currents.

In PUBL. IV we inferred that while there was only little variation in the intensity of the auroral region field-aligned current for positive and zero B_z, for negative B_z, the intensity clearly increased with increasing amplitude of B_z. According to both the component and antiparallel reconnection hypothesis, intensifying negative IMF B_z generally increases the reconnection rate. During positive B_z, component reconnection is caused by B_y, which would imply that the intensity of B_z has no effect on the reconnection rate. According to the antiparallel hypothesis, on the other hand, during positive IMF B_z, reconnection occurs tailward of the cusps. While the reconnection rate should then depend on the B_z amplitude, the ionospheric signatures would be mostly confined to high ($> 80°$) latitudes (e.g., Stauning, 2002), which have not been included in our study. Therefore, our results are in agreement with both hypothesis.

Solar wind dynamic pressure

Due to the pressure balance between the magnetic pressure of the magnetosphere and the mostly dynamic pressure of the solar wind, a pressure pulse in the solar wind compresses the dayside magnetopause. The compression effect travels tailward at the solar wind speed, causing strong auroral activity observable almost instantaneously all around the auroral oval (Zhou and Tsurutani, 2001). Most prominent effects are observed during steady southward IMF (Boudouridis et al., 2003).

In PUBL. IV, we found that with increasing solar wind dynamic pressure, the poleward and equatorward boundaries of the auroral oval moved equatorward and the total field-aligned current intensified linearly with increasing dynamic pressure. While the absolute intensity of the ionospheric currents was stronger during

southward than during northward IMF, the relative change in the intensity of the currents produced by a more intense solar wind dynamic pressure was observed to be approximately the same regardless of the IMF direction. Thus, the most intense currents were obtained with southward IMF and high dynamic pressure.

Merging electric field

The electric field across the reconnected open field lines ($\mathbf{E} = -\mathbf{V}_{sw} \times \mathbf{B}_{IMF}$) maps down to the ionosphere, where it affects the ionospheric currents according to Eq. (1.13) and (1.14). E could be enhanced by increasing B_{IMF} or V_{sw}. Thus, a parameter combining both $\mathbf{B}_{IMF}$ and $\mathbf{V}_{sw}$ would be suitable for describing the geoeffectiveness of the solar wind-magnetosphere coupling.

As shown in PUBL. IV, the merging electric field E_m is such a parameter (Ritter et al., 2004). E_m is defined as

$$E_m = V_{sw}\sqrt{B_y^2 + B_z^2}\sin^2(\theta/2), \tag{5.4}$$

where V_{sw} is the solar wind speed, B_y and B_z are the GSM y and z components of the IMF, and $\theta = \arctan(B_y/B_z)$ is the IMF clock angle. The ratio of the maximum to minimum field-aligned current in the E_m bins was 3.6, while for the dynamic pressure and IMF B_z it was only 2.3 and 3.0, respectively.

5.1.3   Seasonal effects

Seasonal variations in local solar radiation affect the ionospheric conductivity and thereby the intensity of the currents. The difference in the solar radiation between the winter and the summer hemispheres affects mostly conductivity on the dayside. Also particle precipitation varies with season: using global auroral images from the Polar ultraviolet imager in the northern hemisphere during the winter 1996 and the summer 1997, Liou et al. (2001) have shown that compared to winter conditions, nightside auroral precipitation power is suppressed and dayside power enhanced in the summer. Using an MHD simulation, Ridley (2007) demonstrated that if only the solar driven conductance changes were taken into account, the ratio between the maximum summer field-aligned current and maximum winter field-aligned current was about 4. Including a seasonally dependent auroral precipitation to increase the auroral conductance in the winter hemisphere reduced the ratio to 1.6.

Several studies have investigated the seasonal dependence of large-scale field-aligned currents using satellite-based vector magnetic field measurements. Weimer (2001) observed the field-aligned current intensities to be much stronger during summer than winter. According to Papitashvili et al. (2002), the ratio of total

summer/winter field-aligned current is 1.35 and, according to Christiansen et al. (2002), 1.5–1.8. Fujii et al. (1981) and Wang et al. (2005) found the seasonal effect to be confined mainly on the dayside.

We studied the effect in PUBL. IV. In agreement with previous studies, the seasonal effects on the currents were found to be most prominent on the dayside, and the total field-aligned current in the summer was found to be 1.4 times stronger than in the winter. On the dayside (06–18 MLT), the ratio was 1.7 and on the nightside, 1.2.

Due to the effect of the dipole tilt on the magnetospheric configuration, the dayside field-aligned currents move poleward in the summer hemisphere and equatorward in the winter hemisphere, while the nightside field-aligned currents have the opposite seasonal dependence (Ohtani et al., 2005). Over the course of the year, also the orientation of the dipole axis relative to the Sun-Earth line changes. During the equinoxes, when the dipole is tilted along the Earth's orbital track, southward IMF is statistically more likely to occur than during solstices. Hence, the activity level is larger during equinoxes than during solstices (Russell and McPherron, 1973). In PUBL. V, however, we did not see this effect, probably, because only measurements with $K_p < 6$ were included. In PUBL. II, on the other hand, no such limit was set, and the effect was clear.

5.2 Meso-scale ionosphere-magnetosphere coupling

Now that the solar wind conditions producing geomagnetic activity and the large-scale features of substorm evolution are becoming rather well established, the significance of embedded meso-scale (10–1000 km in the ionosphere) structures needs to be understood. In PUBL. III and V, the ionospheric signatures related to two such phenomena, magnetic flux ropes and bursty bulk flows, have been studied. As both are structures occuring in the plasma sheet, this requires simultaneous observations of conjugate magnetospheric and ionospheric regions. Such magnetosphere-ionosphere coupling studies also play a key role in the process of learning to interpret the myriad of signatures on the ionospheric monitor in terms of magnetospheric phenomena.

Locating the ionospheric region conjugate with a magnetospheric phenomenon using a magnetospheric magnetic field model (Sect. 1.5.3) plays an important part for magnetosphere-ionosphere coupling studies. In both cases we have used the T89 model. While the average magnetospheric configurations are quite well represented by the statistical T89 model, the smaller spatial and temporal scale variations associated with substorms cannot be produced (Ganushkina et al., 2004). Field-aligned currents, for instance, can modify the magnetospheric magnetic field structure locally, which may change the mapped footprint. The mapping

can thus fail, if the large-scale magnetospheric configuration is not sufficiently represented by the model, or if the smaller-scale variations not included in the model shift the footprint too much.

However, due to the relatively small amplitude of the ionospheric meso-scale field-aligned currents, any shift in the mapped footprints produced by them should also be small. For instance, Opgenoorth et al. (1994) have demonstrated that in the presence of a localized field-aligned current of 0.3 MA placed around 66°–67° latitude, the actual footprint was shifted a few degrees north of that given by the T89 model. Therefore, the ionospheric signature could be expected to be found near the T89 footprint, if not necessarily at the footprint. Moreover, the spatial and temporal development of the signatures can further be used to confirm the connection.

5.2.1   Bursty bulk flows

Magnetospheric signatures

The plasma flow in the magnetotail plasma sheet is not laminar. While the ambient plasma velocity distribution is very nearly isotropic, the net flow, imposed by the large-scale convection pattern, is composed of short-lived bursts of fast flow. These high-speed (>400 km/s) flows typically appear in about 10-min sequences, called bursty bulk flows (BBF). They consist of several about 1-min velocity enhancements, termed flow bursts (Angelopoulos et al., 1992). Most likely these flows are caused by localized reconnection events. The majority of the flows observed earthward of $x_{GSM} = -20\ R_E$ are directed earthward, and between $-20\ R_E < x < -10\ R_E$ the occurence rate of BBFs decreases substantially with decreasing distance from the Earth, indicating that their source is tailward of or within $x = -20\ R_E$, and that between $-20\ R_E < x < -10\ R_E$ flow braking takes place (Baumjohann et al., 1990). BBFs have a limited dawn-dusk extent of 1–3 R_E (Sergeev et al., 1996; Nakamura et al., 2004) and they are often accompanied by transient magnetic field dipolarisations (Angelopoulos et al., 1992).

The bubble model of Chen and Wolf (1999) describes the basic pattern of how the narrow bursts are connected to the ionosphere. Fig. 5.2 illustrates schematically the plasma flow (black arrows) around a bubble in the plasma sheet and the corresponding convection pattern in the ionosphere (assuming there are no significant potential drops along the magnetic field lines). Although inside the bubble the flow is earthward, the return flow at the dawn and dusk flanks is tailward. In the ionosphere, electric Hall current flows in the opposite direction from the plasma convection. Because the reconnection region is limited in the cross-tail direction, the flow shear between the fast outflow from the reconnection region and the ambient earthward plasma flow within the plasma sheet creates a pair of field-
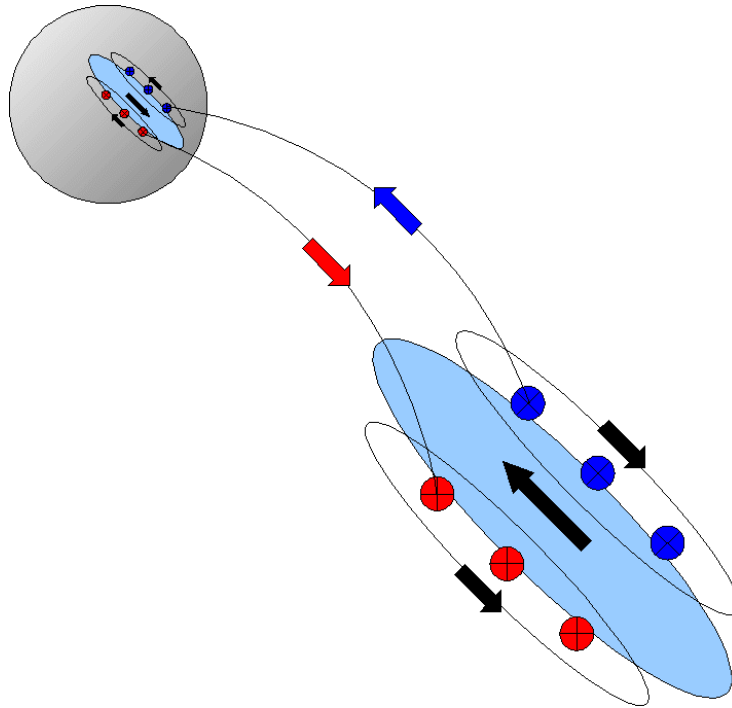
Figure 5.2: Sketch of the plasma flow (black arrows) around a bubble in the plasma sheet and the corresponding convection pattern in the ionosphere. Corresponding to the convection, there is upward field-aligned currents (red) on the duskside and downward field-aligned current (blue) on the dawnside of the bubble. Figure from PUBL. V.

aligned current sheets with upward field-aligned current (red) on the duskside and downward field-aligned current (blue) on the dawnside of the bubble.

Conjugate ionospheric signatures

Auroras are probably so far the most extensively studied form of ionospheric phenomena related to BBFs. Two main kinds of auroral signatures have been observed during BBFs: pseudobreakups and auroral streamers (Nakamura et al., 2001). Pseudobreakups show in global auroral images as a bright spot. The auroral brightness lasts only a few minutes and then fades, or brightens intermittently. Auroral streamers, on the other hand, are approximately north-south aligned, longitudinally narrow auroral forms that first appear at the poleward boundary of the auroral oval and from there expand equatorwards. After reaching the equa-

torward boundary of the oval, they decay by evolving into a patch of diffuse or pulsating aurora. Streamers occur when the auroral oval is wide, both during substorm and non-substorm periods. Both substorm and non-substorm streamers frequently occur in several longitudinal locations of the oval simultaneously, and are often tilted from northwest to southeast (Amm and Kauristie, 2002). Hemispheric north-south conjugacy of streamer-associated precipitation was confirmed by Sergeev et al. (2004). In the schematic picture, the auroral streamer would be associated with the region of upward field-aligned current.

In PUBL. V, we analysed ionospheric equivalent current patterns related to BBFs during Cluster and IMAGE magnetometer network conjunctions between 2001–2006. In order to test the generality of the results of previous event studies (e.g., Kauristie et al., 2003; Hubert et al., 2007; Nakamura et al., 2005), we searched systematically all Cluster-IMAGE conjunctions between 2001–2006 and analysed all 22 BBFs observed during them. The mean duration of the BBFs was 8 min. However, the mean duration of the BBFs observed when the ionospheric footprint of Cluster was located close to the poleward boundary of the auroral oval was clearly longer (17 min) than that of the BBFs observed close to the equatorward boundary of the oval (3 min). This is in agreement with the suggestion that braking of high-speed flows takes place between $-20\ R_E < x < -10\ R_E$: the longer and more efficiently the braking has continued, the smaller the portion of the original high-speed flow which continues to satisfy the definition for a BBF, resulting in shorter observation times.

During 19 out of 22 BBFs, a geomagnetically southeast-northwest aligned, relatively narrow channel of northwestward equivalent current density with downward field-aligned current at its northeastward flank and upward field-aligned current at its southwestward flank was observed in the ionosphere (Fig. 5.3). During the remaining three BBFs, the ionospheric conditions were very quiet and no related signatures were observed.

12 of the BBFs were categorized as substorm-related and 10 as non-substorm-related. A superposed epoch analysis of the IE index revealed a stronger activity level preceding a substorm than a non-substorm BBF. After the BBF observation, however, the activity in both cases was on the same level as that preceding the substorm BBF observation. The observation of the substorm BBF coincided with a substorm-like disturbance in the IE, while the observation of the non-substorm BBF coincided with a step-like increase of the IE. While BBFs could be observed during all phases of the substorm, the superposed epoch analysis agreed with the result of Hubert et al. (2007) that auroral streamers appear often shortly after the substorm onset.

The ionospheric conditions preceding the three BBFs without related ionospheric signatures were clearly more quiet than for the other 19 BBFs. Therefore, it was suggested that if the ionospheric conductivity is small, the cross-tail cur-
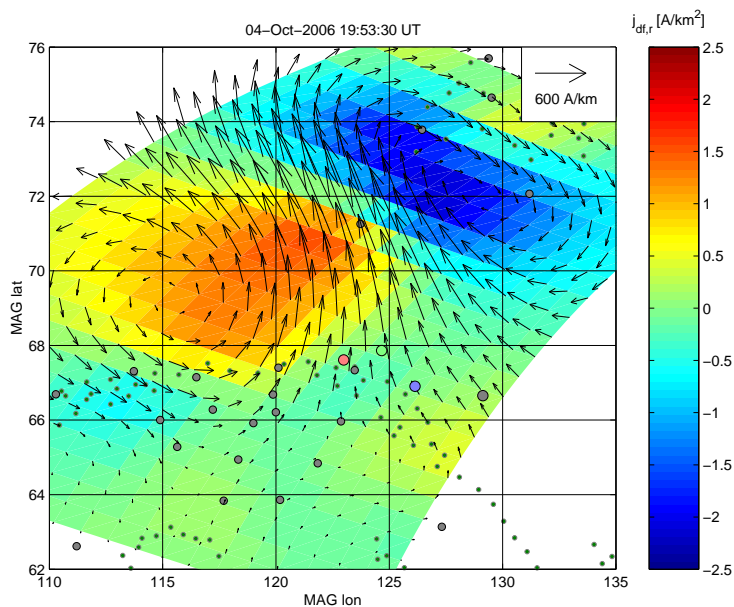
Figure 5.3: Ionospheric equivalent current density, displayed by the black arrows, and its curl, displayed according to the color palette. Sect. 4.2.1 outlines the conditions under which the curl (with the Hall-to-Pedersen conductance ratio $\alpha = 2$) would correspond to the field-aligned current density, with positive currents directed out of the ionosphere. The four dots denote the Cluster footprints and IMAGE magnetometers have been marked by the grey dots. Figure from PUBL. V.

rent that under normal conditions would close through the ionosphere, forming the pair of upward and downward field-aligned current at the flanks of the ionospheric equivalent current channel, might instead prefer to close in the magnetosphere. Normally, the cross-tail current would close partly through the BBF bubble and partly through the ionosphere, depending on their relative conductivities. If the ionospheric conductivity is very smal, however, space charge will accumulate at the flanks of the bubble until the electric field in the bubble is strong enough that the current can close through it. Such a bubble would then probably fill up and disappear quickly.

5.2.2 Flux ropes

Magnetospheric signatures

In the magnetotail plasma sheet, magnetic field signatures involving a bipolar perturbation in GSM B_z, centered on a unipolar perturbation in B_y, have been observed. First-north-then-south B_z signatures are often observed at the leading edge of tailward fast plasma flows, while first-south-then-north signatures are observed at the leading edge of earthward flows. The amplitudes of the perturbations are of the order of about 10 nT, and their duration varies from a few tens of seconds to minutes (Slavin et al., 2003). The signatures are often associated with substorm activity. In the plasma sheet boundary layer and in the lobes, bipolar B_z perturbations without the peak in B_y have also been observed. The two kinds of signatures have been suggested to be related to each other (Slavin et al., 2005), and indeed have been observed simultaneously (Amm et al., 2006b).

The perturbations in the plasma sheet are often interpreted in terms of helical magnetic field structures called flux ropes. A flux rope causes a localized bulge in the plasma sheet. Pinched between the bulging plasma sheet and the magnetopause, the lobe magnetic field intensifies. The region of lobe compression then travels along with the motion of the bulge. These bipolar perturbations are called traveling compression regions (TCR).

The formation of flux ropes can most easily be understood in terms of multiple reconnection X-lines in the near tail, where the simultaneous reconnection of tail field lines at $N + 1$ X-lines leads to the generation of N flux ropes. The reconnection at these multiple X-lines at first involves only closed plasma sheet flux tubes. However, eventually one of the X-lines will outpace the others and begin to reconnect first the outer plasma sheet, then the plasma sheet boundary layer, and finally open lobe flux tubes. This X-line has the role of the classical near-Earth neutral line in the substorm evolution model of Baker et al. (1996). At that point, everything earthward of that X-line will be carried towards the Earth, while everything tailward of it will be swept down the tail (Slavin et al., 2003). The tailward moving flux ropes are often called plasmoid-type while the earthward moving flux ropes are termed BBF-type. According to Hughes and Sibeck (1987), when IMF B_y is positive, also the tail B_y tends to be positive, and the formed flux ropes will have core fields parallel to GSM y. On the other hand, flux ropes formed during negative tail B_y tend to have their core fields antiparallel to y. The central current in the flux ropes has been suggested to flow from dawn to dusk as if the neutral sheet current were locally filamented (Kivelson et al., 1996).

The connection of BBF-type flux ropes to the other parts of the magnetosphere-ionosphere system is still an open question. How does the current through the flux rope close? Through the ionosphere, within the magnetosphere, or in-

terplanetary space? The results of Amm et al. (2006b) indicated that currents in the flux rope and in the ionosphere were in the same direction. Since neither the flux rope nor the ionosphere are current generators, these currents must have been generated elsewhere, possibly in an active reconnection region tailward of the flux rope.

Conjugate ionospheric signatures

Although the ideal force-free flux rope would be detached from the surrounding geomagnetic field lines, a flux rope occurring earthward of a reconnection X-line is embedded in an environment that maps to the ionosphere. In addition to any disturbances caused by the presence of the flux rope on its surroundings, there might be possible ionospheric signatures related to the ends of a non-ideal flux rope.

In PUBL. III, extending the study of Amm et al. (2006b), we examined and compared the possible conjugate ionospheric signatures associated with two flux ropes. Amm et al. (2006b) had found that during the first flux rope, the ionospheric footprint of Cluster coincided with a region of downward field-aligned current. They suggested that this region of downward current, together with a trailing region of upward current further southwestward, might correspond to the ends of the flux rope. Unlike during the first flux rope, however, we did not see any clear ionospheric features associated with the second one. In the GSM xy-plane, the first flux rope axis was tilted with respect to the y direction by $29°$, while the second flux rope axis was almost aligned in the y direction, with an angle of $4°$ only. Therefore, it was suggested that the ground signatures of a flux rope depend on the orientation and the length of the structure.

Chapter 6

Conclusions

6.1 Results

In this thesis, we have studied observationally the solar wind-magnetosphere-ionosphere coupling, with the main focus on the ionospheric currents in the auroral region. The observational data were acquired by the IMAGE magnetometers, CHAMP, the IMAGE satellite, EISCAT, Cluster, ACE and Wind.

Within the framework of this study, a new method for determining the ionospheric currents from low-orbit satellite-based magnetic field data was developed (PUBL. I and II). In contrast to previous techniques, all three current density components can be determined on a matching spatial scale, and the validity of the necessary 1-D approximation, and thus, the quality of the results, can be estimated directly from the data. The method is applicable mostly to electrojet-dominated current distributions, which are inherently 1-D. Such events were shown to be quite common (PUBL. IV).

The new method was employed to derive a way for estimating the Hall-to-Pedersen conductance ratio from ground-based magnetic field data (PUBL. II). The method of characteristics (Amm, 1995), for instance, which is a technique for obtaining ionospheric conductances and currents from ground-based magnetic and ionospheric electric field data, requires an estimate of the conductance ratio. α also provides information on the altitude-dependence of the perpendicular currents: a small α indicates that the ionospheric currents consist mainly of Pedersen currents, while a large α indicates Hall currents. Since Hall currents peak around 110 km altitude and Pedersen currents around 120–130 km altitude, ionospheric currents are thus located on average higher for small than for large α. In addition, the precipitation-related part of α can be used to determine the characteristic energy of electron precipitation in the ionosphere (Robinson et al., 1987).

The 1-D SECS method was also used to investigate the statistical dependence

of the large-scale ionospheric currents on solar wind and geomagnetic parameters. Equations describing the amount of field-aligned current in the auroral region, as well as the location of the auroral electrojets as a function of the K_p index, IMF B_z, solar wind dynamic pressure and the merging electric field, were derived (PUBL. IV).

The meso-scale ionospheric equivalent currents related to two magnetotail plasma sheet phenomena, bursty bulk flows (PUBL. V) and flux ropes (PUBL. III), were studied using the 2-D SECS method. Based on the analysis of 22 events, the typical equivalent current pattern related to bursty bulk flows was established, and it was suggested that the preceding ionospheric conditions play a role in determining the amplitude of the signature. Based on the IE index, the bursty bulk flows were categorised either as substorm or non-substorm related. However, if all the observed earthward bursty bulk flows originated from a near-Earth X-line, they would all by definition have been produced during magnetospheric substorms. Whether the related ionospheric dynamics could be recognised as substorms might then depend on the preceding ionospheric conductivity, for instance. On the other hand, if some of the bursty bulk flows originated from a distant X-line and some from a near-Earth X-line, then the flows could genuinely be divided into two classes: non-substorm related bursty bulk flows originating from a distant X-line and substorm related bursty bulk flows originating from a near-Earth X-line. However, further investigation is needed to either confirm or contradict this. For the flux ropes, on the other hand, only two conjugate events were found. As the equivalent current patterns during these two events were not similar, it was suggested that the ground signatures of a flux rope depend on the orientation and the length of the structure, but analysis of additional events is required to determine the possible ionospheric connection of flux ropes.

6.2   Future directions

Presently, several missions suitable for the study of magnetosphere-ionosphere coupling and ionospheric electrodynamics are either being operated or planned. Several of these produce magnetic measurements that could be analysed using the SECS-based analysis techniques.

NASA's Time History of Events and Macroscale Interactions during Substorms (THEMIS, [14]) is a two-year mission launched in February 2007 consisting of 5 identical spacecraft. The aim of the mission is to distinguish between competing models of substorms. A complementary 2-D ground-based array consists of 20 stations equiped with all-sky imagers and magnetometers is used to determine the location and timing of substorm events. Thus the evolution of the disturbance can be followed in space and time. The 2-D Spherical Elementary Cur-

rent System method can be applied to resolve the ionospheric equivalent current density from ground-based magnetometer measurements. Combining THEMIS stations with other existing networks brings the total number of available magnetometers up to about 100.

The launch of ESA's magnetic field mission Swarm [15], consisting of a constellation of three satellites, is anticipated in July 2011. Two of the satellites will orbit the Earth side-by-side with a 160 km separation at 450 km altitude, and the third satellite at 550 km altitude. All three satellites will provide vector measurements of the magnetic and electric fields. Satellites located closeby will allow for gradients of the fields to be inferred and, thus, the relaxation of the 1-D requirement towards 2-D, when computing ionospheric currents from satellite-based magnetic field. With only two or three satellites, however, the data coverage, particularly in the direction perpendicular to the orbital tracks, may be insufficient for the determination of an arbitrary current system. Therefore, a combination of the 1-D and 2-D SECS techniques, for instance, could be used to derive the ionospheric current density (Amm et al., 2006a). Together with the electric field measurements, the currents can then be used obtain ionospheric conductances from Ohm's law.

With the Cluster mission, the three-dimensional probing of space plasma processes has only begun. Cluster will continue examining the magnetosphere at least until the end of 2009 but, with inter-spacecraft distances between 100 and 10 000 km, it was not designed to study interaction on small scales, nor the interaction between different scales. NASA's Magnetospheric Multiscale (MMS, [16]), consisting of four identical spacecraft in a variably spaced tetrahedron (from 1 km to several R_E), is intended for probing magnetic reconnection sites. The mission confirmation is targeted for July 2009, and the launch is planned for 2014. ESA's Cross-Scale [17], on the other hand, is a candidate mission for investigating the nonlinear dynamics of multi-scale plasma processes, such as shocks, reconnection and turbulence, by simultaneously measuring the space plasma characteristics at the three dominant length scales: electron kinetic scale ($\sim$10 km), ion kinetic scale ($\sim$100–1000 km) and MHD-scale ($\sim$5000–10 000 km). The optimum scientific configuration would be a set of three concentric tetrahedrons – one for each scale.

Bibliography

[01]: http://ccmc.gsfc.nasa.gov/modelweb/models/msis.html
  Cited on 01-Dec-2008.

[02]: http://ccmc.gsfc.nasa.gov/modelweb/models/iri.html
  Cited on 01-Dec-2008.

[03]: http://swdcwww.kugi.kyoto-u.ac.jp/ionocond/sigcal/index.html
  Cited on 01-Dec-2008.

[04]: http://www.space.fmi.fi/MIRACLE/
  Cited on 02-Feb-2009.

[05]: http://www.space.fmi.fi/image/
  Cited on 02-Feb-2009.

[06]: http://www-app2.gfz-potsdam.de/pb1/op/champ/
  Cited on 02-Feb-2009.

[07]: http://www.eiscat.com/
  Cited on 02-Feb-2009.

[08]: http://image.gsfc.nasa.gov/
  Cited on 02-Feb-2009.

[09]: http://clusterlaunch.esa.int/
  Cited on 02-Feb-2009.

[10]: http://www.srl.caltech.edu/ACE/
  Cited on 02-Feb-2009.

[11]: http://www-istp.gsfc.nasa.gov/wind.shtml
  Cited on 02-Feb-2009.

[12]: http://omniweb.gsfc.nasa.gov
  Cited on 02-Feb-2009.

[13]: http://www.spenvis.oma.be/spenvis/help/background/coortran/coortran.html
  Cited on 02-Feb-2009.

[14]: http://www.nasa.gov/themis/
  Cited on 02-Feb-2009.

[15]: http://www.esa.int/esaLP/LPswarm.html
  Cited on 02-Feb-2009.

[16]: http://stp.gsfc.nasa.gov/missions/mms/mms.htm
  Cited on 02-Feb-2009.

[17]: http://sci.esa.int/crossscale/
  Cited on 27-Feb-2009.

Aikio, A. T., Sergeev, V. A., Shukhtina, M. A., Vagina, L. I., Angelopoulos, V., and Reeves, G. D.: Characteristics of pseudobreakups and substorms observed in the ionosphere, at the geosynchronous orbit, and in the midtail, J. Geophys. Res., 104, 12,263–12,287, 1999.

Akasofu, S.-I.: The development of the auroral substorm, Planet. Space Sci., 12, 273–282, 1964.

Allen, J. A. V. and Frank, L. A.: Radiation around the Earth to a radial distance of 107,400 km, Nature, 183, 430–434, 1959.

Allen, J. A. V., Ludwig, G. H., Ray, E. C., and McIlwain, C. E.: Observations of high intensity radiation by satellites 1958 Alpha and Gamma, Jet Propul., 28, 588–592, 1958.

Amm, O.: Direct Determination of the Local Ionospheric Hall Conductance Distribution from Two-Dimensional Electric and Magnetic Field Data: Application of the Method Using Models of Typical Ionospheric Electrodynamic Situations, J. Geophys. Res., 100, 21,473–21,488, 1995.

Amm, O.: Ionospheric elementary current systems in spherical coordinates and their application, J. Geomagn. Geoelectr., 49, 947–955, 1997.

Amm, O. and Fujii, R.: Separation of Cowling channel and local closure currents in the vicinity of a substorm breakup spiral, J. Geophys. Res., 113, doi: 10.1029/2008JA013021, 2008.

Amm, O. and Kauristie, K.: Ionospheric signatures of bursty bulk flows, Surveys in Geophysics, 23, 1–32, 2002.

Amm, O. and Viljanen, A.: Ionospheric disturbance magnetic field continuation from the ground to ionosphere using spherical elementary current systems, Earth Planets Space, 51, 431–440, 1999.

Amm, O., Janhunen, P., Kauristie, K., Opgenoorth, H. J., Pulkkinen, T. I., and Viljanen, A.: Mesoscale ionospheric electrodynamics observed with the MIRACLE network: 1. Analysis of a pseudobreakup spiral, J. Geophys. Res., 106, 24,675–24,690, 2001.

Amm, O., Engebretson, M. J., Hughes, T., Newitt, L., Viljanen, A., and Watermann, J.: A traveling convection vortex event study: Instantaneous ionospheric equivalent currents, estimation of field-aligned currents, and the role of induced currents, J. Geophys. Res., 107, 1334, doi:10.1029/2002JA009472, 2002.

Amm, O., Juusola, L., Viljanen, A., and Kauristie, K.: MIRACLE and CHAMP: Some results; MIRACLE and SWARM: Some opportunities, in: Proc. First SWARM International Science Meeting ESA WPP-261, Nantes, France, 2006a.

Amm, O., Nakamura, R., Frey, H. U., Ogawa, Y., Kubyshkina, M., Balogh, A., and Rème, H.: Substorm topology in the ionosphere during a flux rope event in the magnetotail, Ann. Geophys., 24, 735–750, 2006b.

Angelopoulos, V., Baumjohann, W., Kennel, C. F., Coroniti, F. V., Kivelson, M. G., Pellat, R., Walker, R. J., Lühr, H., and Paschmann, G.: Bursty bulk flows in the inner central plasma sheet, J. Geophys. Res., 97, 4027–4039, 1992.

Axford, W. I. and Hines, C. O.: A unifying theory of high-latitude geophysical phenomena and geomagnetic storms, Can. J. Phys., 39, 1433–1464, 1961.

Baker, D. N., Pulkkinen, T. I., Angelopoulos, V., Baumjohann, W., and McPherron, R. L.: Neutral line model of substorms: Past results and present view, J. Geophys. Res., 101, 12 975–13 010, 1996.

Balogh, A., Carr, C. M., na, M. H. A., Dunlop, M. W., Beek, T. J., Brown, P., on, K.-H. F., Georgescu, E., Glassmeier, K.-H., Harris, J., Musmann, G., Oddy, T., and Schwingenschuh, K.: The Cluster Magnetic Field Investigation: overview of in-flight performance and initial results, Ann. Geophys., 19, 1207–1217, 2001.

Bartels, J., Heck, N. H., and Johnston, H. F.: The three-hour-range index measuring geomagnetic activity, Terr. Magn. Atmos. Electr., 44, 411–454, 1939.

Baumjohann, W., Paschmann, G., and Lühr, H.: Characteristics of high-speed ion flows in the plasma sheet, J. Geophys. Res., 95, 3801–3809, 1990.

Borovsky, J. E., Nemzek, R. J., and Belian, R. D.: The Occurrence Rate of Magnetospheric-Substorm Onsets: Random and Periodic Substorms, J. Geophys. Res., 98, 3807–3813, 1993.

Boudouridis, A., Zesta, E., and Lyons, L. R.: Effect of solar wind pressure pulses on the size and strength of the auroral oval, J. Geophys. Res., 108, 8012, doi: 10.1029/2002JA009373, 2003.

Brekke, A.: Physics of the Upper Polar Atmosphere, Wiley-Praxis Series in Atmospheric Physics, John Wiley and Sons, New York, 1997.

Campbell, W.: Introduction to Geomagnetic fields, Cambridge University Press, Cambridge, 1997.

Chapman, S. and Bartels, J.: Geomagnetism, Oxford University Press, 1940.

Chapman, S. and Ferraro, V. C. A.: A new theory of magnetic storms, 1, The initial phase, J. Geophys. Res., 36, 1931.

Chen, C. X. and Wolf, R. A.: Theory of thin-filament motion in Earth's magnetotail and its application to bursty bulk flows, J. Geophys. Res., 104, 14,613–14,626, 1999.

Christiansen, F., Papitashvili, V. O., and Neubert, T.: Seasonal variations of high-latitude field-aligned currents inferred from Ørsted and Magsat observations, J. Geophys. Res., 107, 1029, doi:10.1029/2001JA900104, 2002.

Davis, T. N. and Sugiura, M.: Auroral electrojet activity index AE and its universal time variations, J. Geophys. Res., 71, 785–, 1966.

Dungey, J. W.: Interplanetary Magnetic Field and the Auroral Zones, Phys. Rev. Lett., 6, 47–48, 1961.

Elphinstone, R. D., Murphree, J. S., Hearn, D. J., Heikkila, W., Henderseon, M. G., Cogger, L. L., and Sandahl, I.: The auroral distribution and its mapping according to substorm phase, J. Atmos. Terr. Phys., 55, 1741–1762, 1993.

Frank, L. A.: On the Extraterrestrial Ring Current During Geomagnetic Storms, J. Geophys. Res., 72, 3753–3767, 1967.

Fujii, R., Iijima, T., Potemra, T. A., and Sugiura, M.: Seasonal Dependence of Large-Scale Birkeland Currents, Geophys. Res. Lett., 8, 1103–1106, 1981.

Fukushima, N.: Generalized theorem for no ground magnetic effect of vertical currents connected with Pedersen currents in the uniform-conductivity ionosphere, Rep. Ionos. Space Res. Japan, 30, 35–40, 1976.

Ganushkina, N. Y., Pulkkinen, T. I., Kubyshkina, M. V., Singer, H. J., and Russell, C. T.: Long-term evolution of magnetospheric current systems during storm periods, Ann. Geophys., 22, 1317–1334, 2004.

Gjerloev, J. W., Hoffman, R. A., Sigwarth, J. B., and Frank, L. A.: Statistical description of the bulge-type auroral substorm in the far ultraviolet, J. Geophys. Res., 112, doi:10.1029/2006JA012189, 2007.

Goldstein, J., Spasojević, M., Reiff, P. H., Sandel, B. R., Forrester, W. T., Gallagher, D. L., and Reinisch, B. W.: Identifying the plasmapause in IMAGE EUV data using IMAGE RPI in situ steep density gradients, J. Geophys. Res., 108, 1147, doi:10.1029/2002JA009475, 2003.

Gonzalez, W. D., Joselyn, J. A., Kamide, Y., Kroehl, H. W., Rostoker, G., Tsurutani, B. T., and Vasyliunas, V. M.: What is a Geomagnetic Storm?, J. Geophys. Res., 99, 5771–5792, 1994.

Gustafsson, G., Papitashvili, N. E., and Papitashvili, V.: A revised corrected geomagnetic coordinate system for Epochs 1985 and 1990, J. Atmos. Terr. Phys., 54, 1609–1631, 1992.

Hedin, A. E.: MSIS-86 Thermospheric Model, J. Geophys. Res., 92, 4649–4662, 1987.

Holme, R., Olsen, N., Rother, M., and Lühr, H.: CO2 – A CHAMP magnetic field model, 220–225, First CHAMP Mission Results for Gravity, Magnetic and Atmospheric Studies edited by C. Reigber and H. Lühr and P. Schwintzer, Springer, Berlin, 2003.

Hubert, B., Kauristie, K., Amm, O., Milan, S. E., Grocott, A., Cowley, S. W. H., and Pulkkinen, T. I.: Auroral streamers and magnetic flux closure, Geophys. Res. Lett., 34, doi:10.1029/2007GL030580, 2007.

Hughes, W. J. and Sibeck, D. G.: On the 3-Dimensional Structure of Plasmoids, Geophys. Res. Lett., 14, 636–639, 1987.

Iijima, T. and Potemra, T. A.: The Amplitude Distribution of Field-Aligned Currents at Northern High Latitudes Observed by Triad, J. Geophys. Res., 81, 2165–2174, 1976.

Kallio, E. I., Pulkkinen, T. I., Koskinen, H. E. J., Viljanen, A., Slavin, J. A., and Ogilvie, K.: Loading-Unloading Processes in the Nightside Ionosphere, Geophys. Res. Lett., 27, 1627–1630, 2000.

Kamide, Y., Perreault, P. D., Akasofu, S.-I., and Winningham, J. D.: Dependence of Substorm Occurrence Probability on the Interplanetary Magnetic Field and on the Size of the Auroral Oval, J. Geophys. Res., 82, 5521–5528, 1977.

Kamide, Y. R. and Brekke, A.: Altitude of the Eastward and Westward Auroral Electrojets, J. Geophys. Res., 82, 2851–2853, 1977.

Kauristie, K., Sergeev, V. A., Amm, O., Kubyshkina, M. V., Jussila, J., Donovan, E., and Liou, K.: Bursty bulk flow intrusion to the inner plasma sheet as inferred from auroral observations, J. Geophys. Res., 108, 1040, doi: 10.1029/2002JA009371, 2003.

Kivelson, M. G. and Russell, C. T.: Introduction to Space Physics, Cambridge University Press, 1995.

Kivelson, M. G., Khurana, K. K., Walker, R. J., Kepko, L., and Xu, D.: Flux ropes, interhemispheric conjugacy, and magnetospheric current closure, J. Geophys. Res., 101, 27,341–27,350, 1996.

Koskinen, H. E. J., Lopez, R. E., Pellinen, R. J., Pulkkinen, T. I., Baker, D. N., and Bösinger, T.: Pseudobreakup and Substorm Growth Phase in the Ionosphere and Magnetosphere, J. Geophys. Res., 98, 5801–5813, 1993.

Kubyshkina, M. V., Sergeev, V. A., and Pulkkinen, T. I.: Hybrid Input Algorithm: An event-oriented magnetospheric model, J. Geophys. Res., 104, 24,977–24,993, 1999.

Liou, K., Newell, P. T., and Meng, C.-I.: Seasonal effects on auroral particle acceleration and precipitation, J. Geophys. Res., 106, 5531–5542, 2001.

Lu, G., Richmond, A. D., Emery, B. A., Reiff, P. H., de la Beaujardière, O., Rich, F. J., Denig, W. F., Kroehl, H. W., Lyons, L. R., Ruohoniemi, J. M., Friis-Christensen, E., Opgenoorth, H., Persson, M. A. L., Lepping, R. P., Rodger, A. S., Hughes, T., McEwin, A., Dennis, S., Morris, R., Burns, G., and Tomlinson, L.: Interhemispheric Asymmetry of the High-Latitude Ionospheric Convection Pattern, J. Geophys. Res., 99, 6491–6510, 1994.

Luhmann, J. G., Walker, R. J., Russell, C. T., Crooker, N. U., Spreiter, J. R., and Stahara, S. S.: Patterns of Potential Magnetic Field Merging Sites on the Dayside Magnetopause, J. Geophys. Res., 89, 1739–1742, 1984.

Lui, A. T. Y., Angelopoulos, V., LeContel, O., Frey, H., Donovan, E., Sibeck, D. G., Liu, W., Auster, H. U., Larson, D., Li, X., Nosé, M., and Fillingim, M. O.: Determination of the substorm initiation region from a ma-

jor conjunction interval of THEMIS satellites, J. Geophys. Res., 113, doi: 10.1029/2008JA013424, 2008.

Marklund, G. T., Karlsson, T., Blomberg, L. G., Lindqvist, P.-A., Fälthammar, C.-G., Johnson, M. L., Murphree, J. S., Andersson, L., Eliasson, L., Opgenoorth, H. J., and Zanetti, L. J.: Observations of the electric field fine structure associated with the westward traveling surge and large-scale auroral spirals, J. Geophys. Res., 103, 4125–4144, 1998.

McPherron, R. L.: Growth phase of magnetospheric substorms, J. Geophys. Res., 75, 5592, 1970.

McPherron, R. L., Russell, C. T., and Aubry, M. P.: 9. Phenomenological Model for Substorms, J. Geophys. Res., 78, 3131–3149, 1973.

Nakamura, R., Baker, D. N., Yamamoto, T., Belian, R. D., III, E. A. B., Benbrook, J. R., and Theall, J. R.: Particle and Field Signatures During Pseudobreakup and Major Expansion Onset, J. Geophys. Res., 99, 207–221, 1994.

Nakamura, R., Baumjohann, W., Brittnacher, M., Sergeev, V. A., Kubyshkina, M., Mukai, T., and Liou, K.: Flow bursts and auroral activations: Onset timing and foot point location, J. Geophys. Res., 106, 10,777–10,789, 2001.

Nakamura, R., Baumjohann, W., Mouikis, C., Kistler, L. M., Runov, A., Volwerk, M., Asano, Y., Vörös, Z., Zhang, T. L., Klecker, B., Rème, H., and Balogh, A.: Spatial scale of high-speed flows in the plasma sheet observed by Cluster, Geophys. Res. Lett., 31, doi:10.1029/2004GL019558, 2004.

Nakamura, R., Amm, O., Laakso, H., Draper, N. C., Lester, M., Grocott, A., Klecker, B., McCrea, I. W., Balogh, A., Rème, H., and André, M.: Localized fast flow disturbance observed in the plasma sheet and in the ionosphere, Ann. Geophys., 23, 553–566, 2005.

Nygrén, T.: Introduction to incoherent scatter measurements, Invers Publications, 1996.

Ohtani, S., Ueno, G., Higuchi, T., and Kawano, H.: Annual and semiannual variations of the location and intensity of large-scale field-aligned currents, J. Geophys. Res., 110, doi:10.1029/2004JA010634, 2005.

Opgenoorth, H. J., Persson, M. A. L., Pulkkinen, T. I., and Pellinen, R. J.: Recovery Phase of Magnetospheric Substorms and its Association With Morning-Sector Aurora, J. Geophys. Res., 99, 4115–4129, 1994.

Papitashvili, V. O., Christiansen, F., and Neubert, T.: A new model of field-aligned currents derived from high-precision satellite magnetic field data, Geophys. Res. Lett., 29, 1683, doi:10.1029/2001GL014207, 2002.

Pulkkinen, A., Amm, O., Viljanen, A., and BEAR Working Group: Ionospheric equivalent current distributions determined with the method of spherical elementary current systems, J. Geophys. Res., 108, 1053, doi:10.1029/2001JA005085, 2003.

Pulkkinen, T. I.: Pseudobreakup or substorm?, in: Proc. Third International Conference on Substorms (ICS-3), pp. 285–293, 1996.

Pulkkinen, T. I.: Space Weather: Terrestrial Perspective, Living Rev. Solar Phys., 4, http://www.livingreviews.org/lrsp-2007-1 (cited on 02-Feb-2009), 2007.

Rème, H., Aoustin, C., Bosqued, J. M., Dandouras, I., Lavraud, B., Sauvaud, J. A., Barthe, A., Bouyssou, J., Camus, T., Coeur-Joly, O., Cros, A., Cuvilo, J., Ducay, F., Garbarowitz, Y., Medale, J. L., Penou, E., Perrier, H., Romefort, D., Rouzaud, J., Vallat, C., Alcaydé, D., Jacquey, C., Mazelle, C., D'Uston, C., Möbius, E., Kistler, L. M., Crocker, K., Granoff, M., Mouikis, C., Popecki, M., Vosbury, M., Klecker, B., Hovestadt, D., Kucharek, H., Kuenneth, E., Paschmann, G., Scholer, M., Sckopke, N., Seidenschwang, E., Carlson, C. W., Curtis, D. W., Ingraham, C., Lin, R. P., McFadden, J. P., Parks, G. K., Phan, T., Formisano, V., Amata, E., Bavassano-Cattaneo, M. B., Baldetti, P., Bruno, R., Chionchio, G., di Lellis, A., Marcucci, M. F., Pallocchia, G., Korth, A., Daly, P. W., Graeve, B., Rosenbauer, H., Vasyliunas, V., McCarthy, M., Wilber, M., Eliasson, L., Lundin, R., Olsen, S., Shelley, E. G., Fuselier, S., Ghielmetti, A. G., Lennartsson, W., Escoubet, C. P., Balsiger, H., Friedel, R., Cao, J.-B., Kovrazhkin, R. A., Papamastorakis, I., Pellat, R., Scudder, J., and Sonnerup, B.: First multispacecraft ion measurements in and near the Earth's magnetosphere with the identical Cluster ion spectrometry (CIS) experiment, Ann. Geophys., 19, 1303–1354, 2001.

Ridley, A. J.: Effects of seasonal changes in the ionospheric conductances on magnetospheric field-aligned currents, Geophys. Res. Lett., 34, doi:10.1029/2006GL028444, 2007.

Ritter, P., Lühr, H., Maus, S., and Viljanen, A.: High-latitude ionospheric crrents durign very quiet times: their characteristics and predictability, Ann. Geophys., 22, 1–14, 2004.

Robinson, R. M., Vondrak, R. R., Miller, K., Dabbs, T., and Hardy, D.: On Calculating Ionospheric Conductances from the Flux and Energy of Precipitating Electrons, J. Geophys. Res., 92, 2565–2569, 1987.

Russell, C. T. and McPherron, R. L.: Semiannual Variation of Geomagnetic Activity, J. Geophys. Res., 78, 92–108, 1973.

Saito, T.: Geomagnetic pulsations, Space Sci. Rev., 10, 319–412, 1969.

Schunk, R. W. and Nagy, A. F.: Ionospheres – Physics, Plasma Physics, and Chemistry, Cambridge Univ. Press, 2000.

Sergeev, V. A., Tanskanen, P., Mursula, K., Korth, A., and Elphic, R. C.: Current Sheet Thickness in the Near-Earth Plasma Sheet During Substorm Growth Phase, J. Geophys. Res., 95, 3819–3828, 1990.

Sergeev, V. A., Pellinen, R. J., and Pulkkinen, T. I.: Steady magnetospheric convection: A review of recent results, Space Science Reviews, 75, 551–604, 1996.

Sergeev, V. A., Liou, K., Newell, P. T., Ohtani, S.-I., Hairston, M. R., and Rich, F.: Auroral streamers: characteristics of associated precipitation, convection and field-aligned currents, Ann. Geophys., 22, 537–548, 2004.

Slavin, J. A., Lepping, R. P., Gjerloev, J., Fairfield, D. H., Hesse, M., Owen, C. J., Moldwin, M. B., Nagai, T., Ieda, A., and Muka, T.: Geotail observations of magnetic flux ropes in the plasma sheet, J. Geophys. Res., 108, 1015, doi: 10.1029/2002JA009557, 2003.

Slavin, J. A., Tanskanen, E. I., Hesse, M., Owen, C. J., Dunlop, M. W., Imber, S., Lucek, E. A., Balogh, A., and Glassmeier, K.-H.: Cluster observations of traveling compression regions in the near-tail, J. Geophys. Res., 110, doi: 10.1029/2004JA010878, 2005.

Sonnerup, B. U. O.: Magnetopause reconnection rate, J. Geophys. Res., 79, 1546–1549, 1974.

Stauning, P.: Field-aligned ionospheric current systems observed from Magsat and Oersted satellites during northward IMF, Geophys. Res. Lett., 29, 8005, doi:10.1029/2001GL013961, 2002.

Sugiura, M.: Hourly values of equatorial Dst for the IGY, Ann. Int. Geophys. Yr., 35, 9–45, 1964.

Tanskanen, E. I., Viljanen, A., Pulkkinen, T. I., Pirjola, R., HÃd'kkinen, L., Pulkkinen, A., and Amm, O.: At substorm onset, 40% of AL comes from underground, J. Geophys. Res., 106, 13,119–13,134, 2001.

Tsyganenko, N. A.: A magnetospheric magnetic field model with a warped tail current sheet, Planet. Space Sci., 37, 5–20, 1989.

Untiedt, J. and Baumjohann, W.: Studies of polar current systems using the IMS Scandinavian magnetometer array, Space Sci. Rev., 63, 245–390, 1993.

Vanhamäki, H., Amm, O., and Viljanen, A.: 1-Dimensional upward continuation of the ground magnetic field disturbance using spherical elementary current systems, Earth Planets Space, 55, 613–625, 2003.

Vanhamäki, H., Amm, O., and Viljanen, A.: Role of inductive electric fields and currents in dynamical ionospheric situations, Ann. Geophys., 25, 437–455, 2007.

Wang, H., LÃijhr, H., and Ma, S. Y.: Solar zenith angle and merging electric field control of field-aligned currents: A statistical study of the Southern Hemisphere, J. Geophys. Res., 110, doi:10.1029/2004JA010530, 2005.

Weimer, D. R.: Maps of ionospheric field-aligned currents as a function of the interplanetary magnetic field derived from Dynamics Explorer 2 data, J. Geophys. Res., 106, 12,889–12,902, 2001.

Zhou, X. and Tsurutani, B. T.: Interplanetary shock triggering of nightside geomagnetic activity: Substorms, pseudobreakups, and quiescent events, J. Geophys. Res., 106, 18,957–18,967, 2001.